PhD Thesis

TOPOLOGICAL OPTICS:
Structured Beam-fields

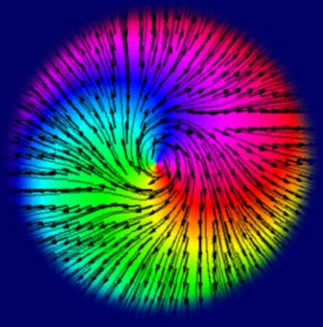

VIJAY KUMAR

School of Physics
University of Hyderabad, India.

TOPOLOGICAL OPTICS:
Structured beam-fields

A thesis submitted during 2014 to the University of Hyderabad in the partial fulfillment of the award of a **Ph.D. degree** in School of Physics

by

VIJAY KUMAR

School of Physics
University of Hyderabad
(P.O) Central University, Gachibowli
Hyderabad – 500 046, India

CERTIFICATE

This is to certify that the thesis entitled **"TOPOLOGICAL OPTICS: STRUCTURES BEAM-FIELDS"** submitted by **VIJAY KUMAR** bearing Regd. No. 09PHPH05 in partial fulfillment of the requirements for the award of **DOCTOR OF PHILOSOPHY** in **PHYSICS** is a bonafide work carried out by him under my supervision and guidance which is a plagiarism free thesis.

The thesis has not been submitted previously in part or in full to this or any other University or Institution for the award of any degree or diploma.

Date: June 2014

Signature of the Supervisor

//Countersigned//

Dean of the School

DECLARATION

I **VIJAY KUMAR** hereby declare that this thesis entitled **"TOPOLOGICAL OPTICS: STRUCTURES BEAM-FIELDS"** submitted by me under the guidance and supervision of Professor **NIRMAL K. VISWANATHAN** is a bonafide research work which is also free from plagiarism. I also declare that it has not been submitted previously in part or in full to this University or any other University or Institution for the award of any degree or diploma. I hereby agree that my thesis can be deposited in Shodganga/INFLIBNET.

Date: June 2014 Name: Vijay Kumar

Signature of the Student
Regd. No. 09PHPH05

Acknowledgements

I take this opportunity to express my gratitude towards my supervisor Prof. Nirmal K. Viswanathan and Giovanni Milione. This thesis is possible only because of the valuable guidance and immense support from my supervisor. He gave me the full freedom to pursue my ideas and always directed me how to bring them in practice. On the other hand brain storming online chatting sessions with Giovanni Milione and his brotherhood had great impact on my thought process and personality.

I like to thank my doctoral committee members, Prof. D. Narayana Rao and Dr. V. S. Ashoka for periodic evaluation of my research work and valuable suggestions.

I owe Prof. A K. Kapoor for the most memorable time of my Ph.D. as his teaching assistant. I am also thankful to Prof. Sir Michael Berry, Prof. E. J. Galvez, Prof. Isaac Freund, Prof. Aleksandr Bekshaev, Dr. Stef Roux, Dr. Mark Dennis and Dr. Florian Flossmann for helping me to understand the emerging field of Singular optics.

I had wonderful and memorable time working with my colleagues, GK (Gopala Krishna), Shankar, Geo, Chandra, Samlan and all the M.Sc. project students. Mr. T. Abraham's excellent quality of office work is highly appreciated. Even the good time spend with my dear friends Abin, Anshuman, Putin and Shiv always re-energizes me to perform best of my ability.

At the end I acknowledge DST for project funding, CSIR and UOH for student fellowship and DST, OSA, ICTP, SPIE, and UPE-2 for travel grants to attend international workshops and conference.

The tribute to

My family

(Rameshwar Dayal, Sunita Devi, Mohan Kumar, Anand Kumar)

and

Giovanni Milione

Table of contents

Abstract

Singularities, where physical quantities are indeterminate and cannot be defined are an integral part of nature. Catastrophe optics deals with the unusual behaviour in the amplitude. Singular optics on the other hand is a study of optical fields with phase and polarization singularities. These singularities may or may not be meaningful, but it invariably is a clue in itself for the underlying interesting phenomena which may produce results of great importance.

This thesis is devoted to singularities in π-symmetric (line) and 2π-symmetric (vector) fields. Singularities in line fields are associated with fundamental ½-index topological structures: lemon, monstar and star. Whereas, radial, node, spiral, circulation and saddle are index-one fundamental topological structures associated with singularities in vector field. Analogous to the Poincaré sphere, topological sphere of ½-index and index-one are theoretically constructed and experimentally realized. These spheres represent all possible symmetric and asymmetric structures achievable in the respective fields, on the surface of the sphere. The ½-index fundamental structures are experimentally realized in the polarization ellipse orientation field using optical fiber and free-space interferometers. Whereas, index-one fundamental structures are experimentally realized in the Poynting vector field, linearly polarized field as well as in the polarization ellipse orientation field. Manifestation of the Pancharatnam-Berry phase and the Gouy phase in polarization topological structured beam-fields are also studied. In addition, the direct and indirect measurements of the Poynting vector in structured beam-fields containing various polarization singularities such as C-point, dipole, C-line are also explored.

Chapter 1

Introduction: Topological structures

Contents

Vijay Kumar under the supervision of Prof. Nirmal K. Viswanathan
School of Physics, University of Hyderabad, India

Chapter

1

Introduction: Topological structures

…singularities…are usually the most important aspects of scalar and vector fields. The physical peculiarities of the problem at hand are usually closely related to the sort of singularities the field has. Likewise, the mathematical properties of the solutions and differential equations are determined by the sort of singularities that the equation and its solution have. Much of our time will be spend in discussing the physical and mathematical properties of singularities in fields.

-Morse and Feshbach, *Methods of theoretical physics*, McGraw-Hill, 1953.

Singularity in physical theories suggests inconsistencies and may or may not be meaningful. But it invariably is a clue itself for the underlying interesting phenomenon which may produce results of great importance. As an example, Nye and Berry in 1973 [1] introduced the phase dislocations or singularities in optical wave. In 1992 Allen et. al. [2–4] associated the angular momentum to this phase singularity thus making the field of S*ingular Optics* more significant and popular. Singularities in line and vector fields can also be associated with topological structures which act as the skeleton and can be used for engineering the optical beam-fields for various applications [5–8].

This chapter will focus on introducing the fundamental topological structures: lemon, monstar, star in π-symmetric fields and radial, node, spiral, circulation, saddle etc in 2π-symmetric fields in optics and nature in general.

1.1. A brief history of light

The history of light dates back to the times of ancient Greeks having evidences of optical illusions, theory of vision, rectilinear propagation of light, phenomena of reflection, metallic mirrors etc. The subsequent civilizations of Romans and Arabs were contented with consolidating the researches of their Greek predecessors. The main contribution of the Arabs in optics comes from Al Hazen (965(?)-1038AD) for performing independent experiments on reflection and refraction [9]. Nearly about the same time the Vikings (700-1100AD) used the polarization of sky light for navigation purposes, which is the first ever historical record of use of polarization of light [10,11]. Roger Bacon (1214(?)-1294AD) a prominent writer of the middle ages, famous for his optics writings, proposed the construction of microscope and telescope, but it was only in the 16th century that the first ever telescope, microscope and spectacle were made [9]. The Snell's law of refraction, Bartholinus' first scientific description of polarization effect of double refraction using Iceland Spar (1669), first attempt to measure velocity of light by Galileo, Huygens wave theory of light, explanation of double refraction using Huygens principle (1672) and Newton's corpuscular theory of light were some of the major discoveries [9–11] of the 17th century. A century later, the Young's double slit experiment (1801) and Fresnel's diffraction theory (1816) proved the wave nature of light, while the Malus discovery of polarization of light using calcite crystal (1808), discovery of Brewster angle (1812) and Fresnel's theoretical explanation of polarization (1821) lead to the wave theory of polarized light [10,11]. Around the same time, in polarization of sky light, Arago (1809), Babinet (1840) and Brewster (1842) discovered the neutral point or point of zero polarization. These neutral points are the first ever historic record of polarization singularities [8,12]. But the light gets its well known electromagnetic nature only after Maxwell provided the mathematical formalism to Faraday's experiments on electromagnetism, resulting in the four Maxwell's equations completely characterizing light [13,14].

1.2. Electromagnetic structure of light

As of now light is treated as an electromagnetic wave. The electric field $\vec{E}$ and magnetic field $\vec{B}$ of the electromagnetic wave in free-space are governed by *Maxwell's equations*:

$$\nabla \cdot \vec{E} = 0;\ \nabla \times \vec{E} = -\frac{\partial \vec{B}}{\partial t}$$
$$\nabla \cdot \vec{B} = 0;\ \nabla \times \vec{B} = \mu_0 \epsilon_0 \frac{\partial \vec{E}}{\partial t} \tag{1.2.1}$$

Now, if we take $\nabla \times \nabla \times \vec{E} = \nabla(\nabla \cdot \vec{E}) - \nabla^2 \vec{E} = \nabla \times -(\partial \vec{B}/\partial t)$, the above four Maxwell's equations reduced to *wave equations*.

$$\nabla^2 \vec{E} = \mu_0 \epsilon_0 \frac{\partial^2 \vec{E}}{\partial t^2} \tag{1.2.2}$$

Similar wave equation can be derived for the magnetic field. The above vector wave equation holds for the components (E_x, E_y) of $\vec{E}$ and are known as *scalar wave equation*. If we assume separable form for the field $E = E_0(x, y, z)e^{-i\omega t}$, we can reduce the time dependency and the wave equation takes the form of *Helmholtz equation*.

$$(\nabla^2 + k^2)E_0 = 0 \tag{1.2.3}$$

Again, assuming $E_0(x, y, z) = u(x, y, z)e^{-ikz}$, the Helmholtz equation reduces to $\frac{\partial^2 u}{\partial x^2} + \frac{\partial^2 u}{\partial y^2} + \frac{\partial^2 u}{\partial z^2} + 2ik\frac{\partial u}{\partial z} = 0$. Under the paraxial approximation $\left|\frac{\partial^2 u}{\partial z^2}\right|^2 \ll \left|2k\frac{\partial u}{\partial z}\right|$ i.e., amplitude variation in the z-direction can be neglected as compared to x and y-directions, we get the well known *paraxial wave equation:*

$$\frac{\partial^2 u}{\partial x^2} + \frac{\partial^2 u}{\partial y^2} + 2ik\frac{\partial u}{\partial z} = 0 \tag{1.2.4}$$

Light of any form i.e. with any kind of distribution of its amplitude, phase and polarization should satisfy the Maxwell's equations. But finding field solutions to Maxwell's equations would be mathematically complicated, therefore the field solutions to paraxial wave equation are more desirable.

1.3. Introducing singularities and topological structures

1.3.1 Topology of phase singularity

The simplest possible solution of the paraxial wave equation is a *plane wave* $u = Ae^{i(\kappa z - \omega t - \varphi_0)}$. Here A and φ_0 are constants, $\kappa = 2\pi/\lambda$ is wave number and $\omega = 2\pi f$ is the angular frequency. Another well know solution to the paraxial wave equation is the Gaussian beam [15]:

$$u = A_0 \frac{W_0}{W(z)} exp\left(-\frac{\rho^2}{W^2(z)}\right) exp\left(-i\kappa z - i\kappa \frac{\rho^2}{2R(z)} + i\zeta(z)\right) \tag{1.3.1}$$

where all the symbols have usual meaning as given in [15]. In Gaussian beam, the intensity profile takes the Gaussian functional form and the phase is constant across the beam cross-section at its waist. The Laguerre-Gaussian (LG) beam [15] is another well known solution of paraxial wave equation in cylindrical coordinates.

$$u_{l,m}(\rho,\phi,z) = A_{l,m} \frac{W_0}{W(z)} \left(\frac{\rho}{W(z)}\right)^{|l|} \mathbb{L}_m^l \left(\frac{2\rho^2}{W^2(z)}\right) exp\left(-\frac{\rho^2}{W^2(z)}\right) \times exp\left(-i\kappa z - i\kappa \frac{\rho^2}{2R(z)} - \underbrace{il\phi}_{\substack{phase\\ vortex}} + i(l+2m+1)\zeta(z)\right) \tag{1.3.2}$$

Consider the LG beams of the form $u_{l,0} \propto \rho^{|l|} e^{-\rho^2} e^{-il\phi} = (x - ily)^{|l|} e^{-\rho^2}$. There is a phase singularity also known as vortex of charge l at the beam centre with index $I = \frac{1}{2\pi}\oint d\phi = \pm 1$. Due to the presence of singularity, the intensity becomes doughnut and phase takes helical topology around the vortex core as shown in Figure 1.3.1. For more details on the physical properties and the generation of optical vortex please refer to [16,17].

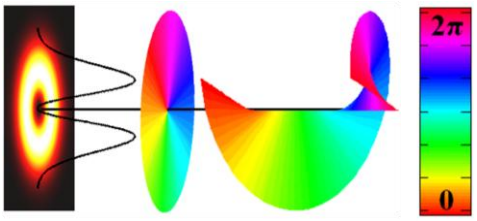

Figure 1.3.1. Topology of phase vortex. First image from left shows the intensity profile of LG beam ($\boldsymbol{u_{1,0}}$) superposed with intensity line profile. Second image is the color coded phase profile across the beam cross-section and the third is the helical phase topology due to phase singularity, as beam propagates in the $\boldsymbol{z}$-direction.

1.3.2 Topology of polarization singularity

In the above section on phase singularity, only scalar fields (wherein polarization is homogeneous across the beam cross-section) is considered. But the scalar fields are not generic and therefore, its vector counterparts have to be considered. Inhomogeneously polarized vector and ellipse fields [18–20] and its singularities, called as *polarization singularities* are more general than phase singularities and act as the skeleton of optical field. This sub-section briefly introduces the polarization singularities in π-symmetric polarization ellipse field and the more details can be found in Chapter 2.

Consider the superposition of orthogonal circularly polarized Gaussian beam (u_{00}) of amplitude ε and the LG beam (u_{l0}) with $l = \pm 1$.

$$\vec{E} = \left[\varepsilon(\hat{x} + i\sigma\hat{y}) + \rho e^{il\phi}(\hat{x} - i\sigma\hat{y})\right]e^{-\rho^2/2W} \tag{1.3.3}$$

Here $\hat{x}, \hat{y}$ are the unit vectors and $\sigma = \pm 1$ is the handedness of circular polarization, such that $\hat{x} \pm i\hat{y} = \hat{e}_{L(R)}$ represents left or right hand circular polarization. If $l\sigma > 0$, lemon (or monstar under special conditions of anisotropic LG) or if $l\sigma < 0$ star patterns will form as shown in Figure 1.3.2(d)-(f). Figure 1.3.2(c) clearly shows a C-point of circular polarization surrounded by polarization ellipses forming a well characterized polarization topological structure. As we move away from the C-point the locus of the equal amplitudes of left circular Gauss and right circular LG beams form a contour of linear polarization known as *L-line*. The C-point and L-line are two types of polarization singularities wherein the polarization ellipse orientation (χ) and normal to polarization ellipse respectively are indeterminate.

C-points are characterized by index $I = \frac{1}{2\pi}\oint d\chi = \pm 1/2$, therefore around the C-point polarization ellipse orientations changes as half of the polar angle (ϕ) i.e. $\chi = \phi/2$. Figure 1.3.2(d)-(f) shows the streamlines (black lines) of χ (families of solutions of $dy/dx = \sin\chi / \cos\chi$) forming lemon, monstar ($I = +1/2$) and star ($I = -1/2$) patterns associated with the C-point. The monstar is distinguished from lemon by the number of straight lines known as *radial line*s ending at C-point, which are three for monstar and star and one for lemon.

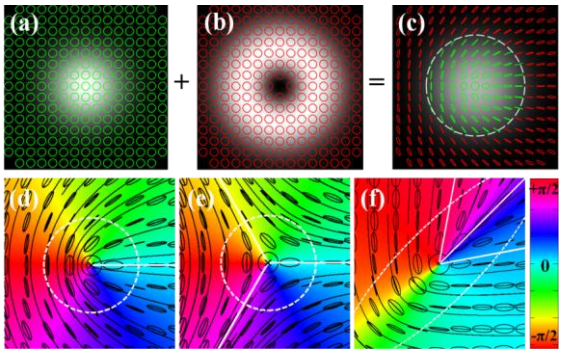

Figure 1.3.2. Topology of polarization singularity. (a) Left circular Gauss, (b) right circular LG and (c) polarization ellipse lemon pattern superposed on the gray scale intensity of the resultant beam. Green and red ellipses represent left and right circular polarization respectively. (d) Lemon, (e) star and (f) monstar patterns formed for different beam combination (Equation (1.3.3). Black contours: polarization ellipses, black cross: C-point, White dotted contour: L-line contour, white solid lines: radial lines ending at the C-point. Background is the color coded ellipse orientation.

The L-line singularity on the other had is the indeterminacy of vector $\hat{n}$, normal to the polarization ellipses. This singularity is characterized by index $I = \pm 1$ and associated with radial, spiral, circulation and saddle topological structures. In this thesis we are not concentrating on L-line singularities, the more details can be found in [21,22].

Now, consider the orthogonal linearly polarized Gaussian and LG beams: $\vec{E} = \left[\varepsilon\hat{x} + \rho e^{i\phi}\hat{y}\right]e^{-\rho^2/2W}$. This beam combination will give rise to a lemon-star pair called a *dipole* as shown in Figure 1.3.3(a). Knowing the fact that orthogonal polarized superposition of Gaussian and LG beams in circular basis will gives isolated C-point while the same in linear basis gives a dipole. Therefore, smoothly varying the polarization basis from circular to linear will transform an isolated C-point to a dipole or vice-versa [23].

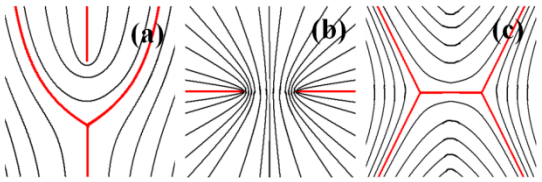

Figure 1.3.3. Polarization singularity topology. (a) lemon-star dipole. (b) lemon-lemon antidipole and (c) star-star antidipole. Orientation of lemon and star in dipole and antidipole are determined by the relative phase between the constituent beams.

Let us consider superposition of orthogonally polarized LG beams with vortex charges $l = \pm 1$:

$$\vec{E} = \left[\{(x - x_0) + il_1 y\}\hat{b}_1 + \{(x + x_0) + il_2 y\}\hat{b}_2\right] e^{-\frac{x^2+y^2}{2W}} \qquad (1.3.4)$$

Here $(\hat{b}_1, \hat{b}_2) \equiv (\hat{e}_L, \hat{e}_R)\ or\ (\hat{x}, \hat{y})$ and x_0 is a constant. Let us first consider the superposition in circular basis. If the superposition is off-axis ($x_0 \neq 0$), it will form dipole for $l_1 = l_2$ and *antidipole* for $l_1 = -l_2$ as shown in Figure 1.3.3. Whereas the on-axis ($x_0 = 0$) superposition will give rise to cylindrical vector beams [24] if and only if $l_1 = -l_2$ which are experimentally realized in Chapter 5. Now consider Equation (1.3.4) in linear basis. For $x_0 = 0$ and $l_1 = -l_2$ will give rise to C-line singularity [18] which are experimentally realized in Chapter 6. For $x_0 \neq 0$ and $l_1 = l_2$ gives a dipole or double-dipole (star-lemon-star) which will be explained in Chapter 3.

1.3.3 A brief history of singular optics

Light treated as an electromagnetic wave is completely characterized by its amplitude, phase and polarization. Nature on the other hand is full of exceptions and singularities are an integral part of it where physical quantities are indeterminate and cannot be defined. *Catastrophe optics* deals with the unusual behaviour of amplitude or intensity [25]. *Singular optics* on the other hand is the study of fields with phase and polarization singularities [16,26]. The first historical account of phase singularity is that of the tidal waves provided by William Whewell [27–29] followed by that of quantal wave function by Dirac [30]. Nye and Berry [1] gave the first consistent theoretical framework to understand the phase singularity in waves which lead to the discovery of orbital angular momentum of light [2], in contrast to the spin angular momentum associated with circular polarization [31]. On the other hand the first historical evidence of polarization singular neutral points goes back to Arago's time [32], measured in sky light polarization followed by polarization singular points in star light [33]. Subsequently, three more neutral points of polarization singularity were discovered [12,34]. Berry, provided the theoretical formalism for the

umbilical points analogous to polarization singular points and associated the three topological structures: lemon, monstar and star [35] which were studied further by Nye and co-workers [21,36,37].

1.4. Topological structures in vector field

Similar to the singularities in π-symmetric polarization ellipse orientation field, singularities in 2π-symmetric vector field (ex. flow or Poynting vector fields) are known as *critical points* characterized by index $I = \pm 1$. These critical points also have associated topological structures: radial, spiral, node, circulation, saddle etc. as shown in Figure 1.4.1. These are fundamental structures of the 2π-symmetric vector fields. In π-symmetric polarization ellipse field, these structures are the first higher order structures and breaks down to a pair of lemon or star under perturbation [38]. A detailed description of the topology of 2π-symmetric vector field and its experimental realization in Poynting vector field, linear polarization field (cylindrical vector beams) and polarization ellipse orientation field (Poincaré beams) can be found in Chapter 5.

The flow field in the neighbourhood of the critical points in a vector field is described by linear stability theory [39]:

$$\begin{bmatrix} V_x \\ V_y \end{bmatrix} = \begin{bmatrix} F_{11} & F_{12} \\ F_{21} & F_{22} \end{bmatrix} \begin{bmatrix} x \\ y \end{bmatrix} \tag{1.4.1}$$

The kind of topological structures around the critical points are determined by the Eigen values of the 2×2 matrix. The structures radial, node, spiral, circulation are characterized by index $I = +1$. Index one structures are further characterized by the number of straight lines known as *radial lines*, ending at critical point [40]. The radial structure has infinite number of radial lines,

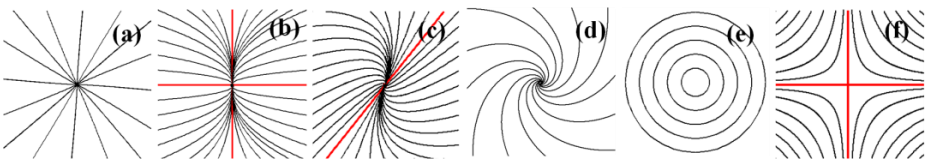

Figure 1.4.1. Topology of vector field. (a) Radial, (b) node, (c) spide, (d) spiral, (c) circulation, (f) saddle. Red lines are the *radial lines* ending at critical point.

node has four, whereas spiral and circulation has none. There is an intermediate structure between node and spiral with two radial lines, which we call *spide* (**spi**ral-no**de**). The radial, spide and circulation are unstable structures which decay into node or spiral upon perturbation. Saddle is the only stable structure characterized by $I = -1$ and with four radial lines as shown in Figure 1.4.1(f).

1.5. Summary

In this chapter we had introduced polarization singularities: C-points which are associated with half-index fundamental topological structures lemon, star and monstar, whereas critical points are associated with integer-index fundamental topological structures radial, spiral, circulation, node and saddle. All these fundamental topological structures act as the skeleton or building blocks of the electromagnetic field. Interestingly, these topological structures are universal and are present in all the branches of science, from finger prints [41,42] to cell arrangements [43,44], from cosmic background radiation [45–49] to gravitational potential [50] and from liquid crystal arrangements [51] to magnetic skyrmions [52] to name a few. These observations inherently tie the singularities and their topologies together and reflect the fact that the underlying physical phenomenons possibly may have common origin to all these systems. Moreover, above examples shows that adopting the topological approach to study complex fields can be more effective than traditional treatments.

The topologically structured optical beam-fields are of current research interest and have the potential for several future applications such as manipulation of optical angular momentum [53–55], plasmonic field engineering [23,56,57], polarization imaging [58,59], superdense information encoding [60], quantum information [61,62] etc.

1.6. References

1. J. F. Nye and M. V. Berry, "Dislocations in Wave Trains," Proc. R. Soc. Lond. A **336**, 165–190 (1974).
2. L. Allen, M. W. Beijersbergen, R. J. C. Spreeuw, and J. P. Woerdman, "Orbital angular momentum of light and the transformation of Laguerre-Gaussian laser modes," Phys. Rev. A **45**, 8185–8189 (1992).
3. L. Allen, M. J. Padgett, and M. Babiker, "The Orbital Angular Momentum of Light," in *Progress in Optics* (Elsevier, 1999), Vol. 39, pp. 291–372.
4. L. Allen, S. M. Barnett, and M. J. Padgett, *Optical Angular Momentum* (Institute of Physics Pub., 2003).
5. D. L. Andrews, *Structured Light and Its Applications* (Academic, 2008).
6. J. P. Torres and L. Torner, *Twisted Photons* (Wiley-VCH, 2011).
7. D. L. Andrews and M. Babikar, *The Angular Momentum of Light* (Cambridge University Press, 2013).
8. G. Horváth and D. Varjú, *Polarized Light in Animal Vision: Polarization Patterns in Nature* (Springer, 2004).
9. Florian Cajori, *History of Physics* (Dover Publications Inc., n.d.).
10. G. P. Konnen, *Polarized Light in Nature* (Cambridge University Press, 1985).
11. "Polarized Light in Nature and Technology," https://www.polarization.com/index-net/index.html.
12. G. Horváth, J. Gál, I. Pomozi, and R. Wehner, "Polarization Portrait of the Arago Point: Video-polarimetric Imaging of the Neutral Points of Skylight Polarization," Naturwissenschaften **85**, 333–339 (1998).
13. J. C. Maxwell, "A Dynamical Theory of the Electromagnetic Field," Philos. Trans. R. Soc. Lond. **155**, 459–512 (1865).
14. J. C. Maxwell, *A Treatise on Electricity and Magnetism* (Oxford : Clarendon Press, 1873).
15. B. E. A. Saleh and M. C. Teich, *Fundamentals of Photonics*, 2 edition (Wiley-Interscience, 2007).

16. M. S. Soskin and M. V. Vasnetsov, "Singular optics," in *Progress in Optics* (Elsevier, 2001), Vol. 42, pp. 219–276.
17. A. M. Yao and M. J. Padgett, "Orbital angular momentum: origins, behavior and applications," Adv. Opt. Photonics **3**, 161–204 (2011).
18. I. Freund, "Polarization singularity indices in Gaussian laser beams," Opt. Commun. **201**, 251–270 (2002).
19. I. Freund, M. S. Soskin, and A. I. Mokhun, "Elliptic critical points in paraxial optical fields," Opt. Commun. **208**, 223–253 (2002).
20. M. R. Dennis, "Polarization singularities in paraxial vector fields: morphology and statistics," Opt. Commun. **213**, 201–221 (2002).
21. J. F. Nye and J. V. Hajnal, "The Wave Structure of Monochromatic Electromagnetic Radiation," Proc. R. Soc. Lond. Math. Phys. Sci. **409**, 21–36 (1987).
22. M. V. Berry, "Index formulae for singular lines of polarization," J. Opt. Pure Appl. Opt. **6**, 675 (2004).
23. S. Pidishety, V. Kumar, and N. K. Viswanathan, "Plasmon-mediated vectorial topological dipole: formation and annihilation," Opt. Lett. **37**, 4233–4235 (2012).
24. Q. Zhan, "Cylindrical vector beams: from mathematical concepts to applications," Adv. Opt. Photonics **1**, 1–57 (2009).
25. M. V. Berry and C. Upstill, "Catastrophe Optics: Morphologies of Caustics and Their Diffraction Patterns," in *Progress in Optics* (Elsevier, 1980), Vol. 18, pp. 257–346.
26. M. R. Dennis, K. O'Holleran, and M. J. Padgett, "Singular Optics: Optical Vortices and Polarization Singularities," in *Progress in Optics* (Elsevier, 2009), Vol. 53, pp. 293–363.
27. W. Whewell, "Essay towards a First Approximation to a Map of Cotidal Lines," Philos. Trans. R. Soc. Lond. **123**, 147–236 (1833).
28. W. Whewell, "Researches on the Tides. Sixth Series. On the Results of an Extensive System of Tide Observations Made on the Coasts of Europe and America in June 1835," Philos. Trans. R. Soc. Lond. **126**, 289–341 (1836).

29. M. R. Dennis, "Topological Singularities in Wave Fields," PhD thesis, University of Bristol (2001).
30. P. a. M. Dirac, "Quantised Singularities in the Electromagnetic Field," Proc. R. Soc. Lond. A **133**, 60–72 (1931).
31. J. H. Poynting, "The Wave Motion of a Revolving Shaft, and a Suggestion as to the Angular Momentum in a Beam of Circularly Polarised Light," Proc. R. Soc. Lond. A **82**, 560–567 (1909).
32. F. Arago, *Oeuvres Complètes de François Arago: Secrétaire Perpétuel de l'Académie Des Sciences* (Gide et J. Baudry, 1854).
33. P. A. G. Scheuer, J. H. Hannay, and P. J. Hargrave, "A note on the interpretation of polarization maps," Mon. Not. R. Astron. Soc. **180**, 163–168 (1977).
34. G. Horváth, B. Bernáth, B. Suhai, A. Barta, and R. Wehner, "First observation of the fourth neutral polarization point in the atmosphere," J. Opt. Soc. Am. A **19**, 2085–2099 (2002).
35. M. V. Berry and J. H. Hannay, "Umbilic points on Gaussian random surfaces," J. Phys. A **10**, 1809–1821 (1977).
36. J. F. Nye, "Lines of Circular Polarization in Electromagnetic Wave Fields," Proc. R. Soc. Lond. A **389**, 279–290 (1983).
37. J. F. Nye, *Natural Focusing and Fine Structure of Light* (Institute of Physics Pub., 1999).
38. T. Delmarcelle and L. Hesselink, "The topology of symmetric, second-order tensor fields," in *Proc. IEEE Conference on Visualization, 1994.* (1994), pp. 140–147.
39. M. Tabor, *Chaos and Integrability in Nonlinear Dynamics: An Introduction* (Wiley, 1989).
40. I. Freund, "Optical Möbius strips in three dimensional ellipse fields: II. Lines of linear polarization," Opt. Commun. **283**, 16–28 (2010).
41. R. Penrose, "The topology of ridge systems," Ann. Hum. Genet. **42**, 435–444 (1979).
42. H. C. Lee and R. E. Gaensslen, *Advances in Fingerprint Technology* (CRC Press, 2001).

43. V. V. Isaeva, N. V. Kasyanov, and E. V. Presnov, "Topological singularities and symmetry breaking in development," Biosystems **109**, 280–298 (2012).
44. L. S. Hirst, A. Ossowski, M. Fraser, J. Geng, J. V. Selinger, and R. L. B. Selinger, "Morphology transition in lipid vesicles due to in-plane order and topological defects," Proc. Natl. Acad. Sci. **110**, 3242–3247 (2013).
45. J. M. Kovac, E. M. Leitch, C. Pryke, J. E. Carlstrom, N. W. Halverson, and W. L. Holzapfel, "Detection of polarization in the cosmic microwave background using DASI," Nature **420**, 772–787 (2002).
46. D. Hanson et.al., "Detection of B-Mode Polarization in the Cosmic Microwave Background with Data from the South Pole Telescope," Phys. Rev. Lett. **111**, 141301 (2013).
47. E. Komatsu, "Matter Adds Twist to Cosmic Microwave Background," Physics **6**, 107 (2013).
48. J. Lizarraga, J. Urrestilla, D. Daverio, M. Hindmarsh, M. Kunz, and A. R. Liddle, "Can Topological Defects Mimic the BICEP2 B-Mode Signal?," Phys. Rev. Lett. **112**, 171301 (2014).
49. A. Moss and L. Pogosian, "Did BICEP2 See Vector Modes? First B-Mode Constraints on Cosmic Defects," Phys. Rev. Lett. **112**, 171302 (2014).
50. V. Vitelli, B. Jain, and R. D. Kamien, "Topological defects in gravitational lensing shear fields," J. Cosmol. Astropart. Phys. **2009**, 034 (2009).
51. X. Shi and Y. Ma, "Topological structure dynamics revealing collective evolution in active nematics," Nat. Commun. **4**, 3013 (2013).
52. N. Nagaosa and Y. Tokura, "Topological properties and dynamics of magnetic skyrmions," Nat. Nanotechnol. **8**, 899–911 (2013).
53. A. Y. Bekshaev and M. S. Soskin, "Transverse energy flows in vectorial fields of paraxial beams with singularities," Opt. Commun. **271**, 332–348 (2007).
54. R. Zambrini and S. M. Barnett, "Angular momentum of multimode and polarization patterns," Opt. Express **15**, 15214–15227 (2007).
55. L.-G. Wang, "Optical forces on submicron particles induced by full Poincaré beams," Opt. Express **20**, 20814–20826 (2012).

56. T.-H. Lan and C.-H. Tien, "Manipulation of the Steering and Shaping of SPPs via Spatially Inhomogeneous Polarized Illumination," Opt. Express **18**, 23314–23323 (2010).
57. T.-H. Lan, C.-Y. Ho, and C.-H. Tien, "Direct measurement of versatile surface plasmon polaritons excited by split polarization," Appl. Phys. Lett. **98**, 081107 (2011).
58. J. S. Tyo, D. L. Goldstein, D. B. Chenault, and J. A. Shaw, "Review of passive imaging polarimetry for remote sensing applications," Appl. Opt. **45**, 5453–5469 (2006).
59. P. C. Brady, K. A. Travis, T. Maginnis, and M. E. Cummings, "Polaro–cryptic mirror of the lookdown as a biological model for open ocean camouflage," Proc. Natl. Acad. Sci. **110**, 9764–9769 (2013).
60. G. Milione, T. A. Nguyen, E. Karimi, D. A. Nolan, S. Slussarenko, L. Marrucci, and R. Alfano, "Superdense Coding with Vector Vortex Beams: A Classical Analogy of Entanglement," in *Frontiers in Optics 2013*, OSA Technical Digest (online) (Optical Society of America, 2013), p. FM3F.4.
61. G. Molina-Terriza, J. P. Torres, and L. Torner, "Twisted photons," Nat. Phys. **3**, 305–310 (2007).
62. E. Nagali, L. Sansoni, L. Marrucci, E. Santamato, and F. Sciarrino, "Experimental generation and characterization of single-photon hybrid ququarts based on polarization and orbital angular momentum encoding," Phys. Rev. A **81**, 052317 (2010).

Chapter 2

Topological structures in π-symmetric fields

Contents

Chapter

2

Topological structures in π-symmetric fields

Topology provides the synergetic means of ascertaining the values of any system of experiences. Topology is the science of fundamental pattern and structural relationship of event constellations.

-Buckminster Fuller, *Operating manual for spaceship earth*, 1968.

In mathematics, topology is the study of complex 2-D and 3-D curves, surfaces, structures etc. The fundamental topological structures in π-symmetric fields are lemon, monstar and star associated with topological index $I = \pm 1/2$. Topological approach to study the complex fields is found to be very useful in understanding the fundamental aspects of the fields. Since it helps in the visualization of distribution of the fields, as a consequence the physical system under consideration can be easily understood. The most exciting thing about the topological studies is the universality of the topological structures which are independent of the physical systems.

This chapter is focus on the theoretical formalism and experimental realization of the complete space of topological structures: symmetric and asymmetric lemon, monstar and star patterns associated with singularities in π-symmetric polarization ellipse orientation field.

TOPOLOGICAL OPTICS: STRUCTURED BEAM-FIELDS

2.1. Introduction

Consider an umbilic point U on the Gaussian random surface Σ, where the two principal curvatures of Σ are equal. Sufficiently close to U, Σ is described as [1]:

$$f(r) = \frac{1}{2}k(x^2 + y^2) + \frac{1}{6}(\alpha x^3 + 3\beta x^2 y + 3\gamma x y^2 + \delta y^3) \qquad (2.1.1)$$

where the coefficients $\alpha, \beta, \gamma, \delta$ of the cubic terms determine the classification of the umbilic point U. Now considering only the cubic part of the above equation in polar angle (χ) for a fixed radius, is written as:

$$f(\chi) = \frac{1}{6}R(\alpha cos^3\chi + 3\beta cos^2\chi \sin\chi + 3\gamma \cos\chi \, sin^2\chi + \delta \sin^3\chi) \qquad (2.1.2)$$

The pattern classification of U falls under three categories: lemon, monstar and star (Figure 2.1.1), depending on the local behavior of the principal axes of curvatures satisfy the condition $df/d\chi = \beta t^3 + (2\gamma - \alpha)t^2 - (2\beta - \delta) - \gamma = 0$ where $t = tan\chi$. The discriminant $D_L = 4[3\gamma(\alpha - 2\gamma) - (\delta - 2\beta)^2\,][3\beta(\delta - 2\beta) - (\alpha - 2\gamma)^2\,] - [(\delta - \beta)(\alpha - \gamma) - 9\beta\gamma]^2$will determine the number of solutions of Equation (2.1.2). If $D_L > 0$ then the pattern is a star or monstar and if $D_L < 0$ then it is a lemon. To distinguish between star and monstar, index I is defined as, $I = \frac{1}{2\pi}\oint \nabla\theta \,.\, dr$, where $tan2\theta = 2(\beta x + \gamma y)/[(\alpha - \gamma)x + (\beta - \delta)y]$ is the rotation of the principle axes. If $I > 0$, the pattern is a lemon or monstar and if $I < 0$ then it is a star.

Similar to this above formalism Thorndike et. al. [2] constructed a tensor matrix in the neighborhood of U and predicted lemon, monstar and star depending on the values of its discriminant D_L and index I.

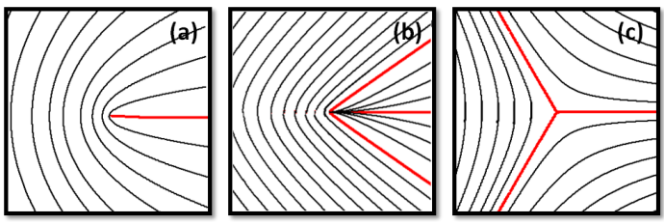

Figure 2.1.1. Topological structures in $\boldsymbol{\pi}$-symmetric polarization ellipse orientation field. (a) Lemon, (b) monstar, and (c) star. Red lines are the radial lines ending at the C-point.

2.2 Topology of polarization ellipse field

The observation of topological patterns in light first started from observation made on skylight [3] followed by in star light [4] and in speckle patterns [5,6]. In 1987 the first attempts towards controllable generation was carried out by Hajnal [7,8] in microwave fields. Thereafter there were few attempts for controllable realization using birefringent crystal [9,10], stressed optical element [11] and liquid crystal q-plates [12]. But none of the methods were able to cover the complete topological space of these patterns as theoretically proposed in [13]. In our quest for experimental realization of the complete space of topological structures, the clue comes from well known work by Nye [14,15], which with the advent of technology available now is easier to realize.

Consider a linear superposition of orthogonal circularly polarized anisotropic vortex and plane wave having a relative phase difference of η:

$$\vec{E} = \left(x + e^{i\alpha}y\right)e^{i\eta}(\hat{x} - i\hat{y}) + (\hat{x} + i\hat{y}) \tag{2.2.1}$$

Here $\alpha = \pi/2(3\pi/2)$ will form isotopic vortex with charge $+1(-1)$, else it is an anisotropic vortex. $\hat{x} \pm i\hat{y} = \hat{e}_{L(R)}$ representing left (L) or right (R) handed circular polarization. Next, we derive the Stokes field $S_{12} = S_1 + iS_2$, where $S_1 = |E_x|^2 + \left|E_y\right|^2$ and $S_2 = 2Re(E_x E_y^*)$ are the Stokes parameters. This Stokes field contains a C-point at $S_{12} = 0$, where the polarization is circular and hence the ellipse orientation $\chi = 0.5 \times \tan^{-1}(S_2/S_1)$ cannot be defined. The L-line contour of linear polarization is found at $S_3 = 2Im\left(E_x E_y^*\right) = 0$. The C-point is surrounded by a well defined ellipse orientation field. The streamlines of ellipse orientations (families of solutions of $dy/dx = \sin\chi / \cos\chi$) will form lemon (or monstar for specific values of η) pattern for $\alpha < \pi$ and $l\sigma > 0$, and star for $\alpha > \pi$ and $l\sigma < 0$ as shown in Figure 2.1.1.

2.3 Lemonstardom

The formation of the topological pattern "monstar" is found to be statistically rare [1,16] as the threshold field anisotropy and phase conditions required for the monstar formation is not easily favorable. Our research group is the first one to realize the monstar in beam-fields in a controllable manner [17,18] in contrast to the speckle field [5,6]. The required conditions for the monstar formation is achieved by superposing two orthogonal Hermite-Gauss (HG) or Laguerre-Gauss (LG) modes. In this section the formation of isolated lemon, monstar and star patterns covering the entire topological space called as *lemonstardom* is explaind, first in the HG spatial mode basis followed by it in the LG spatial mode basis [18].

2.3.1 Superposition of HG modes

The first term of Equation (2.2.1) can be interpreted as superposition of equal amplitude right circular first-order orthogonal HG_{01} and HG_{10} modes having a relative phase of α, representing anisotropic vortex (AV). Consider the generalized expression of Equation (2.2.1) by including the amplitudes $cos\,\psi$ and $sin\,\psi$ for HG_{01} and HG_{10} modes:

$$\vec{E} = (\cos\psi\, x + e^{i\alpha} \sin\psi\, y)e^{i\eta}\hat{e}_R + \hat{e}_L \tag{2.3.1}$$

Considering a special case where the amplitudes of the orthogonal HG modes are equal, $\psi = \pi/4$. For experimental realization using optical fibers this condition can be easily achieved and will be presented in the experimental section. The phase (φ) of the anisotropic vortex (AV) formed due to equal amplitude HG_{01} and HG_{10} modes is given by,

$$\tan\varphi = \frac{Im(AV)}{Re(AV)} = \frac{\tan\eta + \tan\phi\,(\sin\alpha + \cos\alpha\tan\eta)}{1 + \tan\phi\,(\cos\alpha - \sin\alpha\tan\phi)} \tag{2.3.2}$$

Here $\phi = \tan^{-1}(y/x)$ is the polar angle. As we know lemon has one and star, monstar has three radial lines ending at the C-point. The radial lines are straight lines at which ellipse orientation (χ) equal to polar angle (ϕ) i.e.

$\chi = \phi$. Since, phase (φ) varies from $0 - 2\pi$ and the ellipse orientation (χ) varies from $0 - \pi$ implies that $\chi = \varphi/2$. Therefore,

$$\tan 2\phi = \frac{\tan\eta + \tan\phi\,(\sin\alpha + \cos\alpha\tan\eta)}{1 + \tan\phi\,(\cos\alpha - \sin\alpha\tan\phi)} \tag{2.3.3}$$

The above equation can be reduced to cubic equation in $x = tan\phi$

$$\begin{gathered} ax^3 + bx^2 + cx + d = 0 \\ a = \sin\alpha + \cos\alpha\tan\eta \\ b = 2(\cos\alpha - \sin\alpha\tan\eta) + \tan\eta \\ c = 2 + \sin\alpha + \cos\alpha\tan\eta \\ d = \tan\eta \end{gathered} \tag{2.3.4}$$

The determinant Δ of this cubic equation is given by

$$\Delta = 18abcd - 4b^3d + b^2c^2 - 4ac^3 - 27a^2d^2 \tag{2.3.5}$$

If $\Delta \geq 0$ then there exist three roots and hence three radial lines corresponding to monstar ($\alpha < \pi$) or star ($\alpha > \pi$) and if $\Delta < 0$ gives only one root implying one radial line of lemon.

Numerically solving the Equation (2.3.5) for number of radial lines (ϕ) will result in the plot shown in Figure 2.3.1(a). Similarly we can also solve for Equation (2.3.1) numerically, considering $\eta = 0$, shown in Figure 2.3.1(b). These two special cases will be used for experimental realization and represent partial lemonstardom. The whole lemonstardom is covered by solving Equation (2.3.1) considering the parameters (ψ, α, η) as independent.

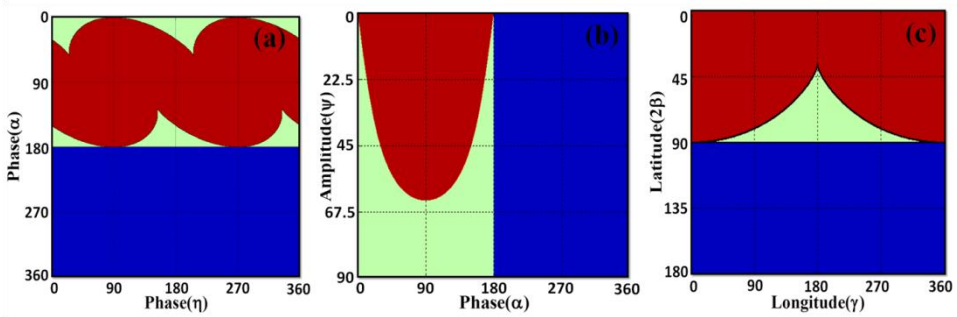

Figure 2.3.1. *Lemonstardom*. (a) Superposition of HG modes for $\boldsymbol{\psi} = \mathbf{45}°$.(b) Superposition of HG modes for $\boldsymbol{\eta} = \mathbf{0}°$. (b) Superposition of LG modes with $\boldsymbol{\delta} = \mathbf{0}°$. Color-representation. red: lemon, green: monstar, blue: star.

2.3.2 Superposition of LG modes

Let us now consider the field due to superposition of right circular anisotropic vortex (AV) formed due to combination of opposite charge isotropic vortices with relative phase γ and left circular plane wave having a relative phase δ:

$$\Psi = \left(\cos\beta r e^{i\phi} + \sin\beta r e^{-i\phi}\, e^{i\gamma}\right) e^{i\delta}\hat{e}_R + \hat{e}_L \tag{2.3.6}$$

This field will form lemons and monstars patterns in polarization ellipse orientations fields for $\beta < \pi/4$ and stars for $\beta > \pi/4$. Monstars are distinguished from the lemons by the number of radial lines. Therefore, solving for the number of radial lines as per the treatment described in the above subsection. The phase (φ) of the anisotropic vortex (AV) formed due to superposition of orthogonal LG modes is equal to two times of ellipse orientation (χ) i.e. $\varphi = 2\chi$. But at the radial lines ellipse orientation (χ) is equal to polar angle (ϕ) i.e. $\chi = \phi$, therefore, we get,

$$\tan 2\phi = \frac{\tan\phi + \tan\beta\,(\sin\gamma - \cos\gamma\tan\phi)}{1 + \tan\beta\,(\cos\gamma + \sin\gamma\tan\phi)} \tag{2.3.7}$$

Similar to that in the above subsection, Equation (2.3.7) can be reduce to cubic equation in $\tan\phi$ and numerical solution for number of radial lines (ϕ) is shown in Figure 2.3.1(c). This represents the whole *lemonstardom* and can also be represented on the sphere as shown in Figure 2.3.2. The role of δ is to shift the origin of the longitude (γ) corresponding to the rotation of the sphere around the polar axis.

2.3.3 C-point sphere

Careful observation of the first term of Equation (2.3.6) shows that, it represents Poincare sphere for orbital angular momentum modes [19,20] containing all possible anisotropic vortices. We know that the superposition of orthogonal circularly polarized vortex and plane waves results in a C-point. Therefore, analogous to the Poincaré sphere we can construct C-point sphere with polar coordinates $(2\beta, \gamma)$ [18] representing all possible C-points on the surface of a sphere as shown in Figure 2.3.2. The lemons are indicated

by the blue region, whereas the monstars occupies a small region of yellow cusp in the northern hemisphere. The whole of southern hemisphere is occupied by the star patterns. The isotropic lemon and star are on the poles and the equator represents a special kind of singularity called as *C-line* singularity. In contrast to C-point where circular polarization is present only at a point, in C-line circular polarization is present along a whole line surrounded by orthogonally oriented ellipses. The astonishing fact about the C-point sphere is that the normalized areas 0.382:0.118:0.5 of lemon : monstar : star comes out be equal to their density fractions of 0.447:0.053:0.5 in random fields [1,16].

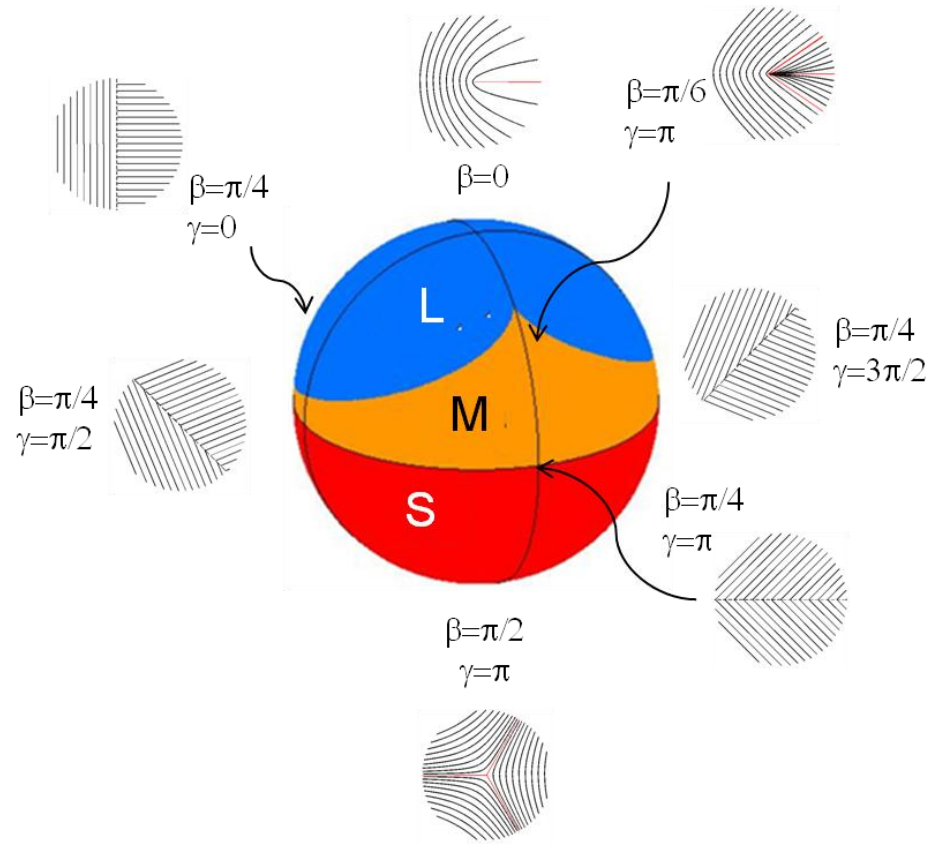

Figure 2.3.2. C-point sphere with polar coordinates are $(2\boldsymbol{\beta}, \boldsymbol{\gamma})$ and (for $\boldsymbol{\delta} = \mathbf{0}$), as specified by Equation (2.3.6). The three colors represents regions of lemons (L):blue, monstars (M):yellow and stars (S):red. Inserts show patterns corresponding to selected points on the sphere.

2.4 Experimental details and results

As mentioed earlier, the experimental realization of *lemonstardom* was never done before and is the focus of this section. Two types of experimental setups were used, one is based on two-mode optical fiber carried at the University of Hyderabad, India and the second is a free-space Mach-Zender interferometer using spatial light modulator carried out in collaboration at the Colgate University, USA [18].

2.4.1 Optical fiber setup

Isolated C-point is achieved as a result of coaxial superposition of orthogonal circularly polarized vortex and plane waves. This condition can be easily achieved in an optical fiber [21–23]. The two-mode optical fiber supports the fundamental mode, which is a plane wave and four eigen vector modes [24]. Selective interference of these modes under desired conditions can form circularly polarized vortex mode which is combines with the fundamental mode giving a C-point at the fiber output. For a brief overview of the fiber modes refer to Appendix A.

The experimental setup for the realization of *lemonstardom* using HG basis is shown in Figure 2.4.1. A circularly polarized He-Ne laser ($\lambda = 632.8\, nm$) is launched into a two-mode optical fiber of length 37.4 cm at an offset skew direction by means of an objective lens (0.4 NA). The output from the fiber is collimated using another objective lens and is made to pass through a half-wave plate (HWP). The final polarization state is diagnosed using the well known Stokes polarimetry technique and is processed to extract the polarization streamlines. A short review of this technique is presented in Appendix B. The input polarization and launching conditions of the fiber controls the relative amplitude (ψ) and phase (α) between the orthogonal HG_{10} and HG_{01}. Therefore careful adjustment of these conditions will excite the appropriate modes required for the generation of C-points at the output. The output half-wave plate is use to control the relative phase (η) between the orthogonal circularly polarized vortex and fundamental modes,

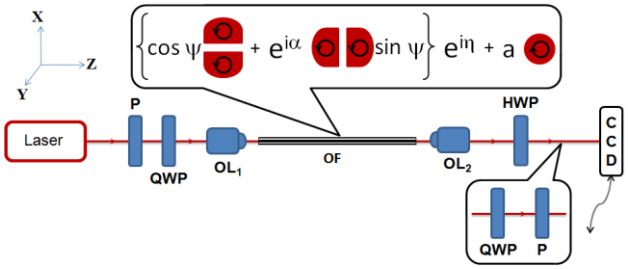

Figure 2.4.1. Optical fiber experimental setup for realization of *lemonstardom* using HG basis (Equation (2.3.1)). P: polarizer, QWP: quarter-wave plate, HWP: Half-wave plate, OL: objective lens, OF: optical fiber.

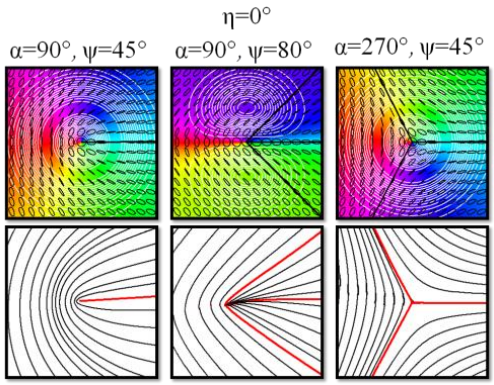

Figure 2.4.2. Experimental results of *lemonstardom* using HG basis (Equation (2.3.1)). 1st, 2nd and 3rd columns are symmetric lemon, monstar and star respectively. First row shows the simulation results. Black small contours are polarization ellipses, white lines are intensity contours, black lines are radial lines and background is color coded ellipse orientation. Second row is the corresponding experimental results.

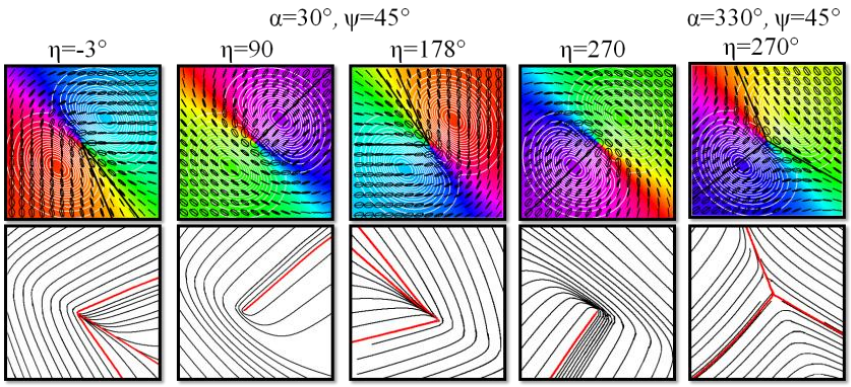

Figure 2.4.3. Experimental results of *lemonstardom* in HG basis (Equation (2.3.1). Asymmetric monstar (1st and 3rd columns), lemon (2nd and 4th columns), star (5th columns). All descriptions are the same as Figure 2.4.2.

which will rotate the pattern. First the launching conditions and input polarization are adjusted to excite the isotropic vortex ($\alpha = 90°$) mode, which in combination with the orthogonal circularly polarized fundamental mode will form a symmetric lemon pattern. Then by rotating the output half wave plate we adjust the relative phase (η) to get the symmetric lemon as shown in Figure 2.4.2. Now translating one of the launching axes we change the amplitudes of the HG_{01} and HG_{10} modes to get an anisotropic vortex required for the monstar formation. Further translating the launching axis will switch the vortex charge [25] and adjusting it further to get isotropic vortex ($\alpha = 270°$) will form the symmetric star. Similar process is adopted to get anisotropic lemons, monstars and stars as shown in Figure 2.4.3. The launching and input polarization are adjusted to get an anisotropic vortex whose intensity contours is an ellipse with ellipticity close to 0.1. Then by rotating the output half wave plate, we adjust the relative phase (η) to rotate the pattern. If the radial line of the lemon coincides with the anisotropic axis of the vortex it will form monstar. Anisotropic stars are also generated in the similar manner.

2.4.2 Free-space setup

The free space co-axial Mach-Zender interferometer used in the laboratory of our collaborator at Colgate University, USA [18] for the realization of *lemonstardom* using Equation (2.3.6) is shown in Figure 2.4.4. Two beams, one with a vortex having phase profile $\varphi(x, y)$ achieved using spatial light modulator and the other with uniform phase Gaussian beam are made to combine using a polarizing beam splitter and is pass through a quarter-wave plate to make their polarization orthogonal circular. PS is the geometric phase shifter element use to adjust the relative phase difference between the two beams. For more experimental details and results refer to [18].

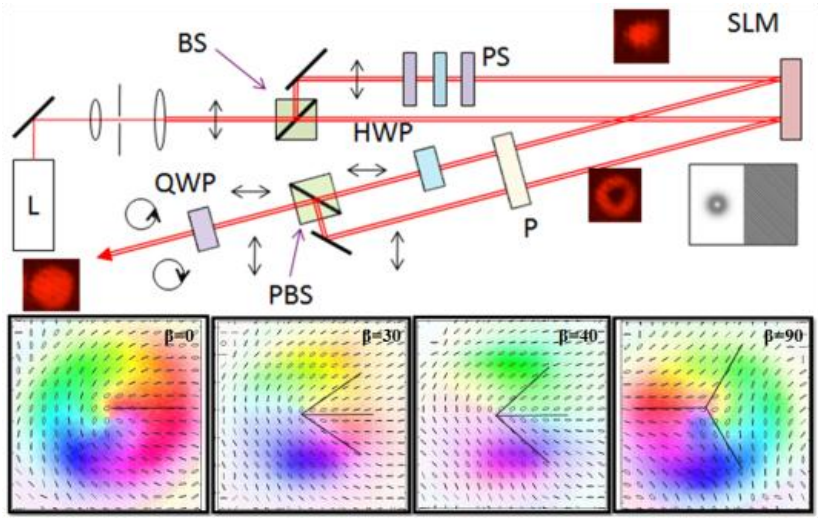

Figure 2.4.4. Free space experimental setup for realization of *lemonstardom* using LG basis (Equation (2.3.6)). L: He-Ne laser, BS: beam splitter, HWP: half wave plate, PS: Pancharatnam-Berry phase shifter, SLM; Spatial light modulator. P: polarizer, PBS: polarizing beam splitter.QWP: quarter wave plate. Bottom row shows the experimental results.

2.5 Summary

Singularities are an integral part of the universe, from large scale cosmic world to small scale quantum world. Singularities in π-symmetric fields are also associated with topological structure lemon, star and monstar. These topological structures act as the skeleton and can be used for optical beam-field engineering. In this chapter theoretical formalism and experimental realization of the complete topological space of structures in π-symmetric optical field is presented. In the optical field these structures are formed due to superposition of vortex and plane waves, which was realized using an optical fiber at University of Hyderabad and equivalent free-space Mach-Zender interferometer method using spatial light modulator at Colgate University. This field manipulation dynamics is global and followed by every system having these structures. Therefore, our results will enable in understanding and manipulating systems with these underlying structures.

This chapter is based on the publication, Physical Review A, **89**, 031801(R) (2014).

2.6 References

1. M. V. Berry and J. H. Hannay, "Umbilic points on Gaussian random surfaces," J. Phys. A **10**, 1809–1821 (1977).
2. A. S. Thorndike, C. R. Cooley, and J. F. Nye, "The structure and evolution of flow fields and other vector fields," J. Phys. A **11**, 1455 (1978).
3. G. Horváth, J. Gál, I. Pomozi, and R. Wehner, "Polarization Portrait of the Arago Point: Video-polarimetric Imaging of the Neutral Points of Skylight Polarization," Naturwissenschaften **85**, 333–339 (1998).
4. P. A. G. Scheuer, J. H. Hannay, and P. J. Hargrave, "A note on the interpretation of polarization maps," Mon. Not. R. Astron. Soc. **180**, 163–168 (1977).
5. V. G. Denisenko, R. I. Egorov, and M. S. Soskin, "Measurement of the morphological forms of polarization singularities and their statistical weights in optical vector fields," J. Exp. Theor. Phys. Lett. **80**, 17–19 (2004).
6. F. Flossmann, K. O'Holleran, M. R. Dennis, and M. J. Padgett, "Polarization Singularities in 2D and 3D Speckle Fields," Phys. Rev. Lett. **100**, 203902 (2008).
7. J. V. Hajnal, "Singularities in the Transverse Fields of Electromagnetic Waves. I. Theory," Proc. R. Soc. Lond. A **414**, 433–446 (1987).
8. J. V. Hajnal, "Singularities in the Transverse Fields of Electromagnetic Waves. II. Observations on the Electric Field," Proc. R. Soc. Lond. A **414**, 447–468 (1987).
9. Y. A. Egorov, T. A. Fadeyeva, and A. V. Volyar, "The fine structure of singular beams in crystals: colours and polarization," J. Opt. A **6**, S217 (2004).
10. F. Flossmann, U. T. Schwarz, M. Maier, and M. R. Dennis, "Polarization Singularities from Unfolding an Optical Vortex through a Birefringent Crystal," Phys. Rev. Lett. **95**, 253901 (2005).
11. A. M. Beckley, T. G. Brown, and M. A. Alonso, "Full Poincare beams," Opt. Express **18**, 10777–10785 (2010).

12. F. Cardano, E. Karimi, L. Marrucci, C. de Lisio, and E. Santamato, "Generation and dynamics of optical beams with polarization singularities," Opt. Express **21**, 8815–8820 (2013).
13. M. R. Dennis, "Polarization singularity anisotropy: determining monstardom," Opt. Lett. **33**, 2572–2574 (2008).
14. J. F. Nye, "Lines of Circular Polarization in Electromagnetic Wave Fields," Proc. R. Soc. Lond. A **389**, 279–290 (1983).
15. J. F. Nye, *Natural Focusing and Fine Structure of Light* (Institute of Physics Pub., 1999).
16. M. R. Dennis, "Polarization singularities in paraxial vector fields: morphology and statistics," Opt. Commun. **213**, 201–221 (2002).
17. V. Kumar, G. M. Philip, and N. K. Viswanathan, "Formation and morphological transformation of polarization singularities: hunting the monstar," J. Opt. **15**, 044027 (2013).
18. E. J. Galvez, B. L. Rojec, V. Kumar, and N. K. Viswanathan, "Generation of isolated asymmetric umbilics in light's polarization," Phys. Rev. A **89**, 031801(R) (2014).
19. M. J. Padgett and J. Courtial, "Poincaré-sphere equivalent for light beams containing orbital angular momentum," Opt. Lett. **24**, 430–432 (1999).
20. A. M. Yao and M. J. Padgett, "Orbital angular momentum: origins, behavior and applications," Adv. Opt. Photonics **3**, 161–204 (2011).
21. V. Kumar and N. K. Viswanathan, "The Pancharatnam–Berry phase in polarization singular beams," J. Opt. **15**, 044026 (2013).
22. V. Kumar, V. V. G. Krishna Inavalli, and N. K. Viswanathan, "Dynamic evolution of transverse energy flow in focused asymmetric optical vector-vortex beams," Opt. Commun. **285**, 4866–4873 (2012).
23. Y. V. Jayasurya, V. V. G. Krishna Inavalli, and N. K. Viswanathan, "Polarization singularities in the two-mode optical fiber output," Appl. Opt. **50**, E131–E137 (2011).
24. A. W. Snyder and J. D. Love, *Optical Waveguide Theory* (Chapman & Hall, 1991).

25. V. V. G. Krishna Inavalli and N. K. Viswanathan, "Switchable vector vortex beam generation using an optical fiber," Opt. Commun. **283**, 861–864 (2010).

Chapter 3

Monstar: Anisotropic lemon

Contents

Chapter

3

Monstar: Anisotropic lemon

Geometry does not teach us to draw these lines, but requires them to be drawn; for it requires that the learner should first be taught to describe these accurately, before he enters upon geometry; then it shows how by these operations problems may be solved.

-Sir Isaac Newton, *Philosophiae naturalis principia mathematica*, 1687.

Singularity in π-symmetric fields are associated with it three distinct topological structures: lemon, monstar and star. Symmetric cases of these structures were first proposed by Berry and Hannay in 1977 [1] and in 2008, Dennis [2] had extended them to include asymmetric cases. Monstar is the intermediate structure having properties of both lemon and star thus it gets its name le**mon**(**star**).

As pointed out in Chapter 2 the monstar structure is statistically rare in natural Gaussian random fields [1,3]. In this chapter focus is on its realization using specially prepared fields and will prove that monstar is anisotropic lemon [2] i.e. monstar can be derived from lemon by squeezing and/or rotation. Two types of mechanisms are used in preparing these special fields. In both the mechanisms superposition of orthogonal linearly polarized vortices beams with a relative phase of $\pi/2$ is used. In one of them, the on-axis superposition of opposite charged vortices is perturbed by circularly polarized Gaussian beam and in the other only off-axis collinear superposition of same charge vortices is considered.

3.1. Is monstar topologically same as lemon?

In the previous chapter the monstar was formed as a superposition of orthogonal circularly polarized anisotropic vortex and uniform phase Gaussian beams which is represented on the C-point sphere. It can be seen that on the longitude $\gamma = \pi$, lemon smoothly transforms to monstar as we vary β form 0 to $\pi/4$ (Figure 2.4.4). In simple words this can be interpreted as squeezing of the lemon structure to form monstar, analogous to squeezing the isotropic vortex to form an anisotropic vortex. The doted circle on the C-point sphere with latitude $\beta = \pi/6$ represents the formation of monstar due to rotation of the lemon structure (Figure 2.4.3). These observations enthused us to the question "Is monstar topologically same as lemon?" since topological properties are invariant under squeezing and rotation. In this chapter the squeezing transformation is explored in two different scenarios. In the first case a monstar dipole (monstar-star pair) is considered and the anisotropy in the polarization ellipse orientation around the monstar is tuned using the star. Similar technique is used in the case of monstar double dipole (star-monstar-star).

3.2. Monstar dipole

In Chapter 2, isolated monstar due to superposition of orthogonal circularly polarized anisotropic vortex and Gaussian beam was considered. This emphasizes that in order to form a monstar, field anisotropy is required i.e. anisotropy in the constituent vortex is used to produce the anisotropy in the polarization ellipse orientation. Alternatively, field anisotropy can be introduced directly in the ellipse orientation field also. In this section a technique suggested by Sir Michael Berry is developed to create the required amount of anisotropy in ellipse orientation field for monstar formation using the superposition of orthogonal linearly polarized opposite charged vortex beams. The idea proposed by Berry in [5] was simplified to realize monstar using specially prepared field. The experimental demonstration of monstar structure realized in a controllable fashion [4] is first of its kind in contrast to

others observing them in speckle fields [6,7]. In this the idea behind this realization is first summarized followed by experimental realization.

3.2.1 Monstar dipole math

Consider the simplify version of Equation (17) of [5] which can be interpreted as on-axis superposition of orthogonal linearly polarized opposite charged vortex beams having a relative phase of $\pi/2$ and perturbed by circularly polarized Gaussian beam [4]:

$$\vec{E}(x,y) = \begin{pmatrix} 1 + b(x+iy) \\ i(1+x-iy) \end{pmatrix} \tag{3.2.1a}$$

$$\vec{E}(x,y) = \begin{pmatrix} 1 \\ i \end{pmatrix} + i(x-iy)\begin{pmatrix} 0 \\ 1 \end{pmatrix} + b(x+iy)\begin{pmatrix} 1 \\ 0 \end{pmatrix} \tag{3.2.1b}$$

Here b is the amplitude of positive charge vortex and is the most important parameter. Now C-point(s) in such a field can be found by setting $\vec{E}\cdot\vec{E} = 0$ [8], which using Equation (3.2.1b) results in $(b-1)[2x + (x^2-y^2)(b+1)] + 2iy[b+1+x(b^2+1)] = 0$. There exists two C-points at $x = y = 0$ and $x = -\frac{2}{b+1}, y = 0$. This implies that the distance between the two C-points decreases as b increase. Out of these two C-points, one of them will be a positive index C-point (lemon or monstar) and other is negative index C-point (star), thus forming a dipole (monstar dipole). Concentrating on the C-point formed at the origin, this is surrounded by polarization ellipses whose local direction of major axis ($\vec{E}_+$) is given as

$$\vec{E}_+ = Re\left[\vec{E}^*\sqrt{\vec{E}\cdot\vec{E}}\right] = k\begin{pmatrix} \cos\gamma \\ \sin\gamma \end{pmatrix} \tag{3.2.2a}$$

$$Re\begin{pmatrix} 1 \\ -i \end{pmatrix}\sqrt{x(b-1)+iy(b+1)} = k\begin{pmatrix} \cos\gamma \\ \sin\gamma \end{pmatrix} \tag{3.2.2b}$$

$$\gamma = \frac{1}{2}\arg\left[x(b-1)+iy(b+1)\right] \tag{3.2.2c}$$

$$\tan 2\gamma = \frac{b+1}{b-1}\tan\phi \tag{3.2.2d}$$

Here k is constant, γ is the angle made by the major axis with the x-axis and $\phi = \tan^{-1}(y/x)$ is the polar angle. Equation (3.2.2d) contains all the required information. If $(b+1)/(b-1)$ is positive, i.e. if b is outside the interval $-1 < b < +1$, γ increases in the same sense as ϕ, implying that the structure

formed is a lemon or monstar. By the similar argument star is formed in the interval $-1 < b < +1$. Discrimination between lemon and monstar is done by line classification i.e. one/three line though the C-point for lemon/monstar. Lines through the origin correspond to $\gamma = \phi$. From Equation (3.2.2d), there is always the line $\gamma = \phi = 0$. Any other line must satisfy $tan^2\,\phi = (3 - b)/(1 + b)$, which cannot be negative and so b must lie in the interval $-1 < b < +3$. But we already know that $-1 < b < +1$ corresponds to star, therefore the interval $+1 < b < +3$ corresponding to monstar and $b < -1, b > 3$ corresponds to lemon. Note that $b = \pm 1$ are the singular cases corresponds to C-line singularities where whole line has circular polarization.

Summarizing the above monstar math we see that the superposition of equal amplitude ($b = 1$) orthogonal linearly polarized vortex beams with relative phase of $\pi/2$ will form a C-line singular polarization pattern, where the polarization is circular along two orthogonal lines (x and y-axis) and the polarization ellipse orientation streamlines in adjacent quadrants making right angles with each other as shown in Figure 3.2.1(a). If we increase to $b = 2$, streamlines squeezes towards the x-axis (Figure 3.2.1(b)) having the right amount of anisotropy for the monstar dipole formation in the presence of right circular Gaussian beam (Figure 3.2.1(c)). Now if we increase to $b = 4$, the distance between the two C-points decreases as a result anisotropy in the polarization ellipse orientation field near the C-points which changes rapidly, transforming the monstar into lemon. This transformation of monstar to lemon can be thought of as squeezing the monstar from the x-directions towards the origin.

3.2.2 Experimental realization of monstar dipole

The experimental setup for the realization of monstar dipole is shown in Figure 3.2.2. Linearly polarized single mode He-Ne laser beam ($\lambda = 632.8\,nm$) is passed through a coaxially aligned double Mach-Zender interferometer. The input beam is split by the beam splitter BS_1 into beam 3 (which is made circularly polarized) and beam 1, and combined at BS_4

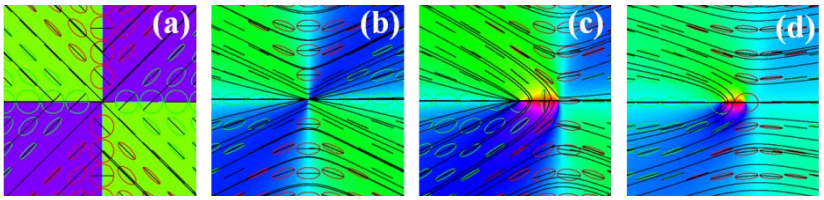

Figure 3.2.1. Simulated monstar dipole. (a) C-line singularity pattern for $\boldsymbol{b} = \mathbf{1}$ as in Equation 3.2.1, (b) Stream line pattern for $\boldsymbol{b} = \mathbf{2}$ without right circular perturbation, (c) Monstar-star dipole for $\boldsymbol{b} = \mathbf{2}$, (d) Lemon-star dipole for $\boldsymbol{b} = \mathbf{4}$.

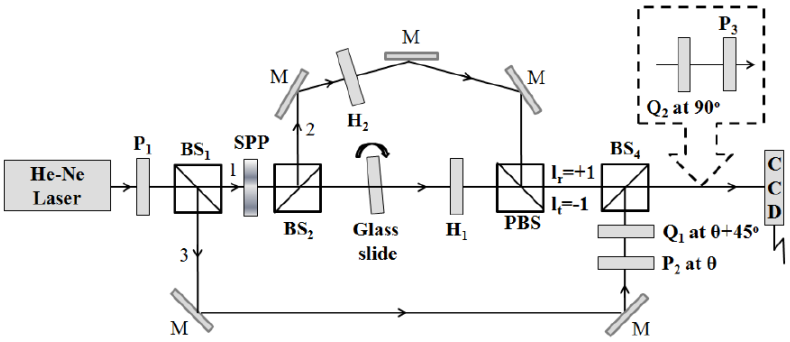

Figure 3.2.2 Experimental setup for monstar dipole. P: polarizers; BS: beam splitters; M: mirrors; SPP: spiral phase plate; H: half-wave plates; PBS: polarizing beam splitter; Q: quarter-wave plates.

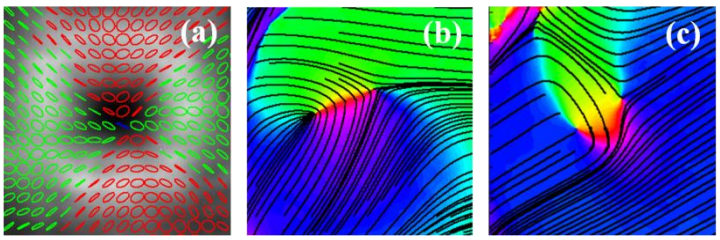

Figure 3.2.3. Experimental results for monstar dipole. (a) Polarization ellipse pattern for $\boldsymbol{b} = \mathbf{2}$ with background as the gray scale beam intensity profile and colour of ellipses represents the handedness. Monstar-star dipole (b) for $\boldsymbol{b} = \mathbf{2}$ and Lemon-star dipole (c) for $\boldsymbol{b} = \mathbf{4}$ with background as colour coded polarization ellipse orientation.

forming the outer interferometer. The beam 1 pass through the spiral phase plate (SPP) forming the vortex beam is spit into transmitted ($\mathbf{I_t}$) and reflected ($\mathbf{I_r}$) vortex beams by BS_2 and combined at the polarizing beam splitter (PBS) forming the inner interferometer. An extra reflection in the reflected beam of the inner interferometer is to invert the charge of the vortex, and half-wave plates H1, H2 and glass slide is use to control the amplitude and relative

phase of the vortex beams. The final polarization state of the beam at the interferometer output is characterized by standard Stokes polarimetry technique and processed further to extract the desire information explained in Appendix A.

First we block the beam 3 and adjust the amplitude ($\boldsymbol{b = 2}$) and phase of the beams in the inner interferometer to get the polarization ellipse pattern as shown in Figure 3.2.3(a). After releasing beam 3 we get monstar-star dipole as shown in Figure 3.2.3(b). We then adjust the amplitude to $\boldsymbol{b = 4}$ forming the lemon-star dipole as in Figure 3.2.3(c). The deviations from the expected plots are due to the errors in the adjustments of amplitude and phase of the superposed beams.

3.3. Monstar double-dipole

In this section another technique to create the right amount of polarization ellipse field anisotropy for monstar formation directly in the ellipse orientation field is demonstrated. Consider the collinear superposition of two orthogonal linearly polarized vortex beams of same charges and having relative phase of $\pi/2$, whose vortices are displaced along the x-axis by $2x_a$, where x_a is constant.

$$\vec{E}(x,y) = \left[\{(x+x_a)+iy\}\begin{pmatrix}0\\1\end{pmatrix} + i\{(x-x_a)+iy\}\begin{pmatrix}1\\0\end{pmatrix}\right] e^{-\frac{r^2}{2w}} \qquad (3.3.1)$$

Figure 3.3.1(a) shows the simulated plot of Equation 3.3.1 for $x_a/w = 0.5$. It clearly shows a star-lemon-star double dipole with three C-points. The centre structure is always at the origin which is lemon and the adjacent two are stars present along the x-axis at the intersection of the line profile of the constituent vortex beams beyond $x = \pm x_a$ as shown in Figure 3.3.1(b). Increasing the displacement between the vortices to $x_a/w = 1$, it is found that the central lemon transforms to a monstar as shown in Figure 3.3.1(c). In other words as we increase the displacement between the orthogonally polarized vortices the central C-point remains at the origin and the neighbouring C-points move away stretching the central lemon resulting it in a monstar. This is equivalent to squeezing in the y-direction towards the origin.

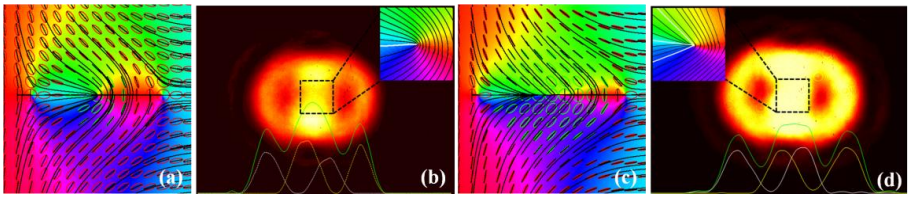

Figure 3.3.1. Monstar double dipole. (a) Simulated plot of star-lemon-star double dipole as describe by Equation 3.3.1 for $\boldsymbol{x_a/w = 0.5}$ and star-monstar-star double dipole for $\boldsymbol{x_a/w = 1}$ (c). (b) and (d) are the corresponding experimental beam intensity (hot scale) with line profiles passing through origin. White, yellow and green curves are the line profiles of the constituent vortex beams and the resulting beam through the vortices along the $\boldsymbol{x}$-axis respectively. Insert shows the experimentally measured lemon and monstar patterns in the dotted box. Adjacent stars are not observed in the experimental data since the intensity is too weak to observe them.

The experimental setup for the realization of double dipole is shown in the Figure 3.3.2. Linearly polarized vortex beams formed after the spiral phase plate is fed into the Mach-Zender interferometer which is coaxially align in the beginning. Using mirror M_2 and the polarizing beam splitter (PBS) we displace the vortex beams horizontally and collinearly align as shown in Figure 3.3.2. After the PBS, the vortex beams are orthogonal linearly polarized and horizontally displaced collinearly propagating beams which is made to pass through a combination of quarter-half-quarter plates acting as Pancharatnam-Berry phase shifter to adjust the relative phase. Polarization diagnosis of the desired beam is performed using imaging Stokes polarimetry.

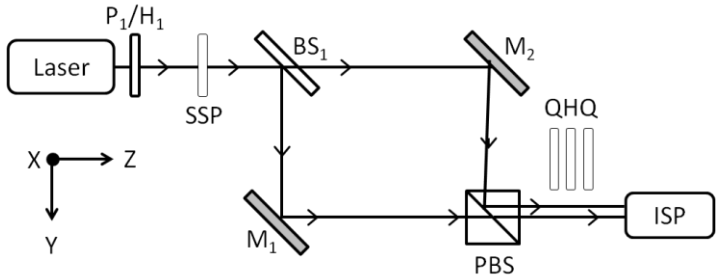

Figure 3.3.2. Experimental setup for the realization of monstar double dipole. ISP: imaging Stokes polarimeter, QHQ is the Pancharatnam-Berry phase shifter and all elements are same as in Figure 3.2.2.

Figure 3.3.1(b) shows the experimental data for star-lemon-star double dipole. White, yellow and green curves are the line profiles of the constituent vortex beams and the resulting beam through the vortices along the **x**-axis respectively.Three C-points are present at the intersections of the line profile of the constituent vortex beams. Insert shows the lemon present pattern in the dotted box. Adjacent stars are not observed in the experimental data since the intensity is too weak to observe them. If we further displace the beams and align them collinearly we find the central lemon transform to monstar as shown in Figure 3.3.1(d) proving the fact that right amount of stretch or squeezing of lemon introduces the required amount of anisotropy in the polarization ellipse orientation field for the monstar formation.

3.4. Summary

In this chapter it was shown that the monstar structure though being statistically rare in random Gaussian fields but can be experimentally realized in specially prepared optical fields by means of superposition of vortex beam(s) and uniform phase Gaussian beams under appropriate phase and polarization conditions. It was also shown that monstar is topologically the same as lemon structure via three different examples and prove that lemon and monstar can smoothly transform to each other under rotation, squeezing and stretching transformations. One important point still need to be addressed is that monstar being topologically the same as lemon then why there is any need to define line classification to distinguish monstar? In order to look for an answer it is necessary to find a physical situation where these two structures show their clear cut signatures.

The central idea of this chapter is yet to be published but some of the results are taken from the publication: Journal of Optics, **15**, 044027 (2013).

3.5. References

1. M. V. Berry and J. H. Hannay, "Umbilic points on Gaussian random surfaces," J. Phys. A **10**, 1809–1821 (1977).
2. M. R. Dennis, "Polarization singularity anisotropy: determining monstardom," Opt. Lett. **33**, 2572–2574 (2008).
3. M. R. Dennis, "Polarization singularities in paraxial vector fields: morphology and statistics," Opt. Commun. **213**, 201–221 (2002).
4. V. Kumar, G. M. Philip, and N. K. Viswanathan, "Formation and morphological transformation of polarization singularities: hunting the monstar," J. Opt. **15**, 044027 (2013).
5. M. V. Berry, "Geometry of phase and polarization singularities illustrated by edge diffraction and the tides," in *Proc. SPIE* (2001), Vol. 4403, pp. 1–12.
6. V. G. Denisenko, R. I. Egorov, and M. S. Soskin, "Measurement of the morphological forms of polarization singularities and their statistical weights in optical vector fields," J. Exp. Theor. Phys. Lett. **80**, 17–19 (2004).
7. F. Flossmann, K. O'Holleran, M. R. Dennis, and M. J. Padgett, "Polarization Singularities in 2D and 3D Speckle Fields," Phys. Rev. Lett. **100**, 203902 (2008).
8. M. V. Berry, "Index formulae for singular lines of polarization," J. Opt. Pure Appl. Opt. **6**, 675 (2004).

TOPOLOGICAL OPTICS: STRUCTURED BEAM-FIELDS

Chapter 4

Manifestation of Pancharatnam-Berry topological phase

Contents

Vijay Kumar under the supervision of Prof. Nirmal K. Viswanathan
School of Physics, University of Hyderabad, India

Chapter

4

Manifestation of Pancharatnam-Berry topological phase

…Hence we will be guilty of no internal inconsistency if we make the following statement by way of a definition: the phase advance of one polarized beam over another (not necessarily in the same state of polarization) is the amount by which its phase must be retarded relative to the second, in order that the intensity resulting from their mutual interference may be a maximum.

-S. Pancharatnam, *Proc. Indian Acad. Sci.*, 44, 252 (1956).

Polarization topological structured beam-fields wherein polarization is space variant and the polarization ellipses form half-index topological structures in the beam cross-section. Due to continuously changing polarization states in the beam, *Pancharatnam-Berry topological phase* becomes the inherent property of the polarization topological structured beams.

In this chapter one of the manifestations of the *Pancharatnam-Berry topological phase* is explored via selective polarization interference in polarization topological structured beams with lemon and dipole topological structures in the polarization ellipse orientation field. We find that the polarization topological structured beams are a 'sea' of component vortices of scalar fields of all polarization states on the Poincaré sphere.

TOPOLOGICAL OPTICS: STRUCTURED BEAM-FIELDS

4.1. Introduction

S. Pancharatnam in 1956 was the first to observe the evidence of topological (geometrical) phase during his study on crystal optics [1] well known by his name as *Pancharatnam phase*. He discovered the non-transitive property of polarization i.e. a polarization state under cyclic transformation will acquire an extra phase. Unaware of the work of Pancharatnam Sir Michael Berry in 1984 independently discovered [2] "Quantal phase factor accompanying adiabatic changes" popularly known as *Berry phase.* In contrast to *Pancharatnam phase* defined for light polarization, *Berry phase* is universal, applies to any state undergoing adiabatic changes. Soon after the discovery of Berry topological phase, one of the manifestations: *Spin redirected phase* acquired by polarization state when it is transported around a closed path in momentum space was theoretically and experimentally observed [3,4]. Once Berry came to know about Pancharatnam's work, immediately the connection between the two was established and Pancharatnam's work interpreted as the optical analogue of Aharonov-Bohm effect [5]. Thus, now the phase accompanying cyclic or non-cyclic changes in the polarization state of light is known as *Pancharatnam-Berry topological phase* (PBTP). Interested readers are advised to follow the monogram [6] for a good collection of papers on topological phase, its foundation, manifestations and applications till late 1980's. In addition to *Pancharatnam phase* and *spin redirection phase* other manifestations of topological phase are also observed. *Lorentz-group Berry phase* [7] and *modal transformation phase* [8,9] arises due to cyclic Lorentz transformations in squeezed state of light and modal transformations of the higher order Gaussian modes respectively. The recently discovered *higher-order Pancharatnam-Berry phase* for spatially inhomogeneous vector light beams arises due to the vector mode transformation [10,11].

Some of the most important applications of topological phase are frequency and phase shifters [12,13]. The well known spatial light modulator (SLM) extensively used for amplitude and phase modulation were initially based on the phase shifter for pure amplitude [14], pure phase [15] or two

level $(0-\pi)$ phase [16] modulation. Moreover space-variant polarization manipulation having immense potential for future application and can be easily achieved using subwavelength structured based Pancharatnam-Berry phase optical element [17] or by using liquid crystal based Q-plate [18,19]. Interestingly, for both technologies, PBTP is the underlying physical principle. It was also shown that geometric phase can also be use to in quantum computation as topological phase gates [20].

In this chapter we will present manifestations of PBTP in polarization topological structured beams with lemon and dipole structures, generated using a two-mode optical fiber (TMF) [21]. A two beam Mach-Zehnder type interferometer is constructed in which the signal arm is where we use a TMF to generate the required polarization topological structured beams by launching polarized Gaussian beam. The reference arm of the interferometer is a Gaussian beam having all possible polarization state achieved using a Q-H wave plate combination. We observe that due to interference between like polarizations the reference beam polarization governs the trajectory of the component vortices in the beam cross-section, clearly indicating the contribution of variable PBTP in the formation of polarization topological structured beams.

4.2. Experimental details

Schematic of the experimental setup used to observe the manifestation of Pancharatnam–Berry topological phase in topologically structured beams is shown in Figure 4.3.1. A He–Ne laser operating at 632.8 *nm* is polarized in the vertical direction using a Glan–Thompson polarizer. Two beam splitters (BS) and mirrors (M) are used to construct a two beam Mach–Zehnder type interferometer. In the transmitted arm of the Mach–Zehnder interferometer a quarter-wave plate (Q1) is introduced to launch circularly polarized light into the two-mode fiber of length 37.4 cm using a 20x microscope objective lens (L_1). The input end of the fiber is positioned using a three-axis precision stage to launch the laser beam at an offset-skew angle to excite the desired modes

in the fiber. The fiber output is collimated using another 20x microscope objective (L_2). In the reference arm a quarter-wave plate–half-wave plate (Q3-H) combination is kept to achieve all possible states of the polarization. A spatially resolved, point-wise polarization ellipse map of the fiber output is constructed via imaging Stokes polarimetry carried out using a quarter-wave plate–polarizer (Q4-P) combination and a CCD camera as describe in Appendix B.

4.3. Results and discussion

4.3.1 'Sea' of component vortices

Launching a linear vertically polarized Gaussian beam from the He–Ne laser as an off-axis skew beam into the two-mode optical fiber excites co-propagating orthogonal linear polarized Gaussian (LG_{00}) and Laguerre–Gauss (LG_{01}) modes in the fiber. These mode combination leads to the formation of a vectorial topological dipole (Figure 4.3.2(d)) in polarization ellipse orientation field. The dipole is formed due to the superposition of vertically polarized ($S_1 = +1,\ S_2 = S_3 = 0$) Gaussian and horizontally polarized ($S_1 = -1,\ S_2 = S_3 = 0$) Laguerre–Gauss modes. It is possible to generate an isolated C-point singularity surrounded by lemon (Figure 4.3.2(a)) or star topological pattern from this dipole by passing it through a quarter-wave plate whose optic axis makes an $\pi/4$ or $-\pi/4$ with vertical direction. This will convert the orthogonal linear to orthogonal circular polarization states. Consider the lemon pattern formed due to the superposition of a right circular ($S_3 = +1,\ S_1 = S_2 = 0$) plane wave and a left circular ($S_3 = -1,\ S_1 = S_2 = 0$) polarized vortex wave. If we consider the interference of this lemon pattern with right circularly polarized reference plane wave, no forklet is observed in the interference pattern. However, interference with left circular plane wave will show a clear forklet pattern almost at the center of the beam, corresponding to the phase dislocation in the projected field of the vector-vortex beam shown in the inserts of Figure 4.3.2(a). This difference in the interference fringe pattern is due to the fact that orthogonal polarizations do not interfere

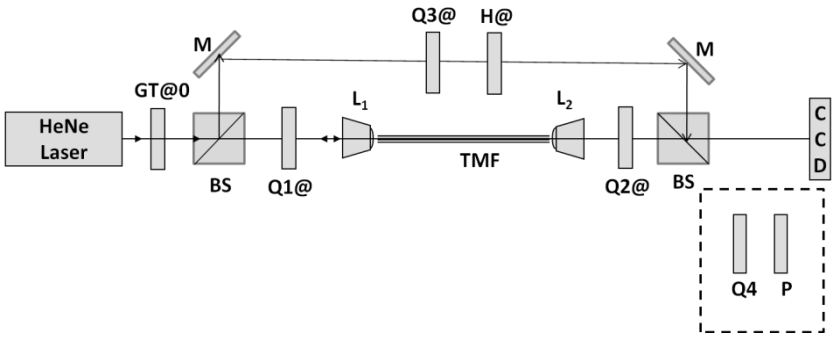

Figure 4.3.1. Experimental setup for the observations of the manifestations of the Pancharatnam-Berry topological phase. GT: Glan-Thompson polarizer, BS: 50-50 Beam splitter, M: Mirror, Q: Quarter-wave plate, H: Half-wave plate, L: Microscope objective lens, P: Polarizer, CCD: Detector camera.

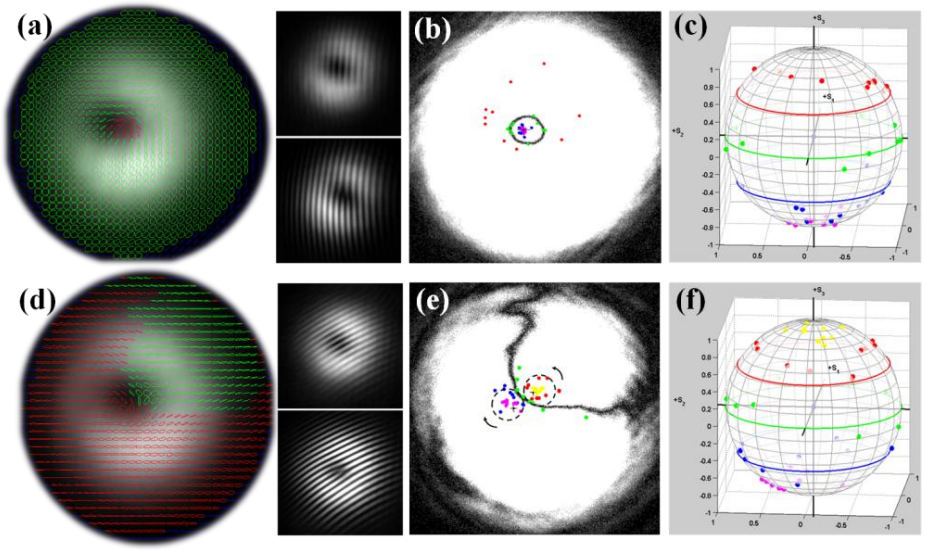

Figure 4.3.2. Experimental results. (a) Lemon and (d) Topological dipole overlapped on the gray scale intensity profile. Inset shows the interference patterns of the constituent modes. (b) and (e) shows the contours of component vortices for topological patterns shown in (a) and (d) respectively. Magenta: $S_3 = -1$; blue: $S_3 = -0.5$; green: $S_3 = 0$; red: $S_3 = +0.5$; yellow: $S_3 = +1$, plus: C-points; black line: L-contour. (c) and (f) shows the component vortex points shown in (b) and (e) are plotted on the Poincaré sphere with the corresponding theoretically expected trajectories respectively.

and like polarizations interfere giving maximum contrast fringes. If we interfere the lemon pattern with a reference plane wave whose polarization lies on the different latitude planes on the Poincaré sphere with $S_3 = \pm 0.5$ and 0, which is achieved here by the Q-H wave-plate combination in the reference arm. The forklet position makes closed contours in the beam cross-section which increase in size from $S_3 = -0.5$ to $+0.5$ as shown in Figure 4.3.2(b). In this case forklet rotates on the contour in the clockwise direction.

The lemon vector beam-field and the reference beam-field can be described as

$$\vec{E}_{lemon} = [\varepsilon + (x + iy)]\hat{x} + [i\varepsilon - i(x + iy)]\hat{y} \tag{4.3.1}$$

$$\vec{E}_{refrence} = A_x\hat{x} + A_y e^{i\phi}\hat{y} \tag{4.3.2}$$

where ε is the plane wave amplitude forming the lemon pattern, A_x, A_y are the amplitudes of x and y components and ϕ is the relative phase between them. Interfering the lemon pattern with a reference plane wave beam is equivalent to computing its field projection in the direction of the reference wave. $Re(\vec{E}^*_{refrence} \cdot \vec{E}_{lemon}) = Im(\vec{E}^*_{refrence} \cdot \vec{E}_{lemon}) = 0$ will give the vortex positions in the field of the lemon pattern projected on the reference beam polarization and the locus of the vortex positions forms a closed contour around the C-point as shown in Figure 4.3.2(b). These vortices are called component vortices since these are phase singular points in the component fields of vector field. For $\phi = \pi/2$ and $A_x = A_y$ the reference beam picks the C-point and for $\phi = 0$ the reference beam polarization lies on the equator of the Poincaré sphere with $S_3 = 0$, therefore the locus of the vortex positions is identical to the L-contour. The lemon pattern therefore can be considered as a 'sea' of phase vortices in the field whose polarization is represented on the Poincare sphere except with $S_3 = +1, S_1 = S_2 = 0$.

Similar observations are carried out for the star topological structure as well. In this case also the forklet position forms closed contours in the beam cross-section but rotates in the anticlockwise direction and increasing in its size from $S_3 = +0.5\ to\ -0.5$. There is no phase singularity in the field when $S3 = -1, S1 = S2 = 0$.

Now consider a vectorial topological dipole formed due to superposition of vertical polarized fundamental mode and horizontal polarized Laguerre-Gauss mode as shown in Figure 2d. The forklet movement in the beam cross section now forms two sets of contours (Figure 2e), one for lemon and another for star and their individual behavior is similar to the ones described above. This dipole field has no phase singularity, only in the projected field with $S_1 = +1, S_2 = S_3 = 0$.

4.3.2 Pancharatnam-Berry topological phase

The value of the Stokes parameters at the forklet positions plotted on the Poincaré sphere tracks the same trajectory as that of the reference beam polarization as shown in Figure 4.3.2(c) and (f). This shows that polarization states lying on the contours acquires same amount of Pancharatnam-Berry topological phase as the reference beam polarization. The deviations between the experimental and theoretical trajectories can be attributed to different parts of the beam has traversed different paths as it propagates through the fiber in contrast to the simple on-axis superposition using free-space optical components.

4.4. Summary

The formation of polarization topological structured beams with lemon, star and dipole topological structures in the polarization ellipse field is presented. The presence of C-point singularity leads to a systematic distribution of polarization states around it giving rise to variable Pancharatnam-Berry topological phase on closed contours in the beam cross-section. This topological phase is responsible for the creation of component vortices in the scalar fields whose polarization states lie on the Poincaré sphere. Our experimental measurements using the Q-H combination tracks the fork position forming contours by picking the same value of Stokes parameters as of the reference arm polarization and thus the states on the contours acquire the same amount of Pancharatnam-Berry topological phase

as that of the reference beam. Thus polarization topological structured vector beam-fields is a 'sea' of phase singular points of the scalar fields whose polarization states lies on the Poincaré sphere due to the acquired Pancharatnam-Berry topological phase. The use of this approach based on selective interference of polarization topological structured beams may be helpful for exploring the phase acquired due to path dependent spin and spin-dependent path as the beam travels through the two mode fiber [22].

This chapter is based on the publication, Journal of Optics, **15**, 044026 (2013).

4.5. References

1. S. Pancharatnam, "Generalized theory of interference, and its applications," Proc. Indian Acad. Sci. - Sect. A **44**, 247–262 (1956).
2. M. V. Berry, "Quantal Phase Factors Accompanying Adiabatic Changes," Proc. R. Soc. Lond. Ser. Math. Phys. Sci. **392**, 45–57 (1984).
3. R. Y. Chiao and Y.-S. Wu, "Manifestations of Berry's Topological Phase for the Photon," Phys. Rev. Lett. **57**, 933–936 (1986).
4. A. Tomita and R. Y. Chiao, "Observation of Berry's Topological Phase by Use of an Optical Fiber," Phys. Rev. Lett. **57**, 937–940 (1986).
5. M. V. Berry, "The Adiabatic Phase and Pancharatnam's Phase for Polarized Light," J. Mod. Opt. **34**, 1401–1407 (1987).
6. A. Shapere and F. Wilczek, *Geometric Phases in Physics* (World Scientific, 1989).
7. R. Y. Chiao and T. F. Jordan, "Lorentz-group Berry phases in squeezed light," Phys. Lett. A **132**, 77–81 (1988).
8. S. J. van Enk, "Geometric phase, transformations of gaussian light beams and angular momentum transfer," Opt. Commun. **102**, 59–64 (1993).
9. E. J. Galvez, P. R. Crawford, H. I. Sztul, M. J. Pysher, P. J. Haglin, and R. E. Williams, "Geometric Phase Associated with Mode Transformations of Optical Beams Bearing Orbital Angular Momentum," Phys. Rev. Lett. **90**, 203901 (2003).

10. G. Milione, H. I. Sztul, D. A. Nolan, and R. R. Alfano, "Higher-Order Poincaré Sphere, Stokes Parameters, and the Angular Momentum of Light," Phys. Rev. Lett. **107**, 053601 (2011).
11. G. Milione, S. Evans, D. A. Nolan, and R. R. Alfano, "Higher Order Pancharatnam-Berry Phase and the Angular Momentum of Light," Phys. Rev. Lett. **108**, 190401 (2012).
12. R. Bhandari, "Polarization of light and topological phases," Phys. Rep. **281**, 1–64 (1997).
13. P. Hariharan, "The geometric phase," in *Progress in Optics*, E. Wolf, ed. (Elsevier, 2005), Vol. Volume 48, pp. 149–201.
14. G. D. Love and J. Gourlay, "Intensity-only modulation for atmospheric scintillation correction by liquid-crystal spatial light modulators," Opt. Lett. **21**, 1496–1498 (1996).
15. M. O. Freeman, T. A. Brown, and D. M. Walba, "Quantized complex ferroelectric liquid crystal spatial light modulators," Appl. Opt. **31**, 3917–3929 (1992).
16. S. E. Broomfield, M. A. A. Neil, E. G. S. Paige, and G. G. Yang, "Programmable binary phase-only optical device based on ferroelectric liquid crystal SLM," Electron. Lett. **28**, 26–28 (1992).
17. E. Hasman, G. Biener, A. Niv, and V. Kleiner, "Space-variant polarization manipulation," in *Progress in Optics*, Emil Wolf, ed. (Elsevier, 2005), Vol. 47, pp. 215–289.
18. L. Marrucci, C. Manzo, and D. Paparo, "Optical Spin-to-Orbital Angular Momentum Conversion in Inhomogeneous Anisotropic Media," Phys. Rev. Lett. **96**, 163905 (2006).
19. B. Piccirillo, V. D'Ambrosio, S. Slussarenko, L. Marrucci, and E. Santamato, "Photon spin-to-orbital angular momentum conversion via an electrically tunable q-plate," Appl. Phys. Lett. **97**, 241104 (2010).
20. D. Leibfried et.al., "Experimental demonstration of a robust, high-fidelity geometric two ion-qubit phase gate," Nature **422**, 412–415 (2003).
21. V. Kumar and N. K. Viswanathan, "The Pancharatnam–Berry phase in polarization singular beams," J. Opt. **15**, 044026 (2013).

22. A. Y. Savchencko and B. Y. Zel'dovich, "Wave propagation in a guiding structure: one step beyond the paraxial approximation," J. Opt. Soc. Am. B **13**, 273 (1996).

Chapter 5

Topological structures in 2π-symmetric fields

Contents

Vijay Kumar under the supervision of Prof. Nirmal K. Viswanathan
School of Physics, University of Hyderabad, India

Chapter

5

Topological structures in 2π-symmetric fields

By topology we mean the doctrine of the modal features of objects, or of the laws of connection, of relative position and of succession of points, lines, surfaces, bodies and their parts, or aggregates in space, always without regard to matters of measure or quantity.

- Johann Benedict Listing, *Vorstudien zur Topologie* (1847).

Recent project on "Background Imaging of Cosmic Extragalactic Polarization (BICEP)-2" experimentally confirm the "Big- Bang" theory by adopting topological approach for polarization in cosmic background radiation [1–3]. On a different scale, the study of topological arrangement of cells give vital information regarding the infections [4,5]. These recent studies clearly show the effectiveness of adopting topological approach in a large variety of physical systems. The first step towards that direction is to understand all possible topological structures and its dynamics in the field under study. Similar to Chapter 1 the focus of this chapter is to develop a unified model of fundamental symmetric and asymmetric topological structures in the 2π-symmetric fields.

5.1. Introduction

Topological approach to study physical system is fast becoming popular and useful to unravel its several aspects. Experimental confirmation of "Big-Bang" theory using polarization topological patterns in the cosmic background radiation [1–3], colloidal systems [6], magnetic skyrmions [7], laser processing [8], biological systems [9,4] etc. are few examples. In order to successfully apply topological approach to different physical systems we should first have consistent and unified model of all possible topological structures in a given field, which is the aim of this chapter.

Any vector is 2π-symmetric and the corresponding field is called 2π-symmetric vector field. Complex optical vector fields, wherein the distribution of field parameters is also complex in nature renders it difficult to study such systems. Identifying the organising centres or the critical or fixed points, known as singular points in such complex vector fields, which gives a structure to its surrounding thus acting like a skeleton. Thus, makes the analysis of complex optical vector fields much easier. A brief review of the linear stability theory [10] is presented here which will give all the possible topological structures around critical points. The vector flow close to the critical point can be represented by general second order differential equations: $\dot{x} = f(x, y)$ and $\dot{y} = g(x, y)$. Critical points (x_0, y_0) are identified as $\dot{x} = \dot{y} = 0$. The evolution of the flow $(\delta x, \delta y)$ in the neighbourhood of the critical point can then be written as a power of $\delta x, \delta y$. Therefore,

$$\delta\dot{x} = f_x(x_0, y_0)\delta x + f_y(x_0, y_0)\delta y + f_{yx}(x_0, y_0)\delta x\delta y + \cdots \qquad (5.1.1a)$$

$$\delta\dot{y} = g_x(x_0, y_0)\delta x + g_y(x_0, y_0)\delta y + g_{yx}(x_0, y_0)\delta x\delta y + \cdots \qquad (5.1.2b)$$

under first order approximation the above equations can be written as:

$$\frac{d}{dt}\begin{bmatrix}\delta x\\ \delta y\end{bmatrix} = \begin{bmatrix} f_x(x_0, y_0) & f_y(x_0, y_0)\\ g_x(x_0, y_0) & g_y(x_0, y_0)\end{bmatrix}\begin{bmatrix}\delta x\\ \delta y\end{bmatrix} \qquad (5.1.3)$$

The solution of the above equation is the linear superposition of the eigen values ($\boldsymbol{\lambda}$) of the $\mathbf{2} \times \mathbf{2}$ matrix (M) and its corresponding eigen vectors ($\vec{\boldsymbol{D}}$):

$$\delta\vec{X} = c_1\vec{D}_1 e^{\lambda_1 t} + c_2\vec{D}_2 e^{\lambda_2 t} \qquad (5.1.4)$$

here $\boldsymbol{c_1 and\ c_2}$ are arbitrary coefficients, and the eigen values are the roots of $\boldsymbol{det|M - \lambda I| = 0}$, where *I* is the unit matrix.

The results of the linear stability theory are as follows, for

1. $\lambda_1 < \lambda_2 < 0$ & $\lambda_1 > \lambda_2 > 0$ $\Rightarrow$ node
2. $\lambda_1 < 0 < \lambda_2$ $\Rightarrow$ saddle
3. $\lambda_1 = \pm\alpha + i\beta$ & $\lambda_2 = \pm\alpha - i\beta (\alpha, \beta > 0)$ $\Rightarrow$ spiral
4. $\lambda_1 = i\omega$ & $\lambda_2 = -i\omega$ $\Rightarrow$ elliptic point

If the eigen values are degenerate i.e. if $\lambda_1 = \lambda_2 = \lambda$, then the type of critical point is determined by the sign and nature of the eigen vectors $\vec{D}_1$ and $\vec{D}_2$.

5. $\vec{D}_2 = 0$ & $\lambda \lesseqgtr 0$ $\Rightarrow$ radial

All possible topological structures around the organizing centers in a vector field are shown in Figure 5.3.1.The critical points having generic structures which are stable under perturbations are spiral, node and saddle which can be easily seen in a variety of physical systems in nature.

5.2. Stokes field topology

The aim of this chapter is also to have a unified picture of topological structures in 2π-symmetric vector fields, similar to that of Chapter 2 for π-symmetric fields. To move forward in that direction the 2π-symmetric Stokes field $S_{12} = S_1 + iS_2$ gives an important clue. Consider Stokes vortex or Poincaré vortex [11] derived as an argument of the Stoke field S_{12}: $\Phi_{12} = arg(S_1 + iS_2)$. We know that polarization ellipse orientation is given by: $\chi = 0.5 \times \tan^{-1}(S_2/S_1) \Rightarrow \Phi_{12} = 2\chi$. Therefore, if we construct streamlines (Appendix B) in a fixed coordinate system, factor half transforms the half-index topological structures lemon, star, monstar in π-symmetric polarization ellipse orientation field into radial (or spiral or circulation), saddle, node in 2π-symmetric Stokes vortex field respectively as shown in Figure 5.2.1. We can see that if we locally rotate the ellipses forming the lemon topological pattern the whole lemon pattern rotates (Figure 5.2.1(a)-(c)) in the ellipse orientation field whereas corresponding pattern in the Stokes vortex field transform form radial to spiral to circulation (Figure 5.2.1 (a′)-(c′)).

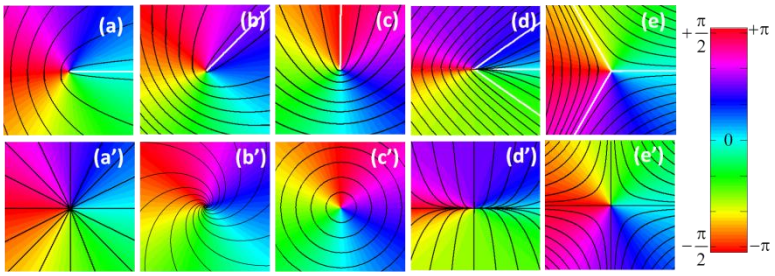

Figure 5.2.1. Fundamental topological structures. (a)-(c)lemons, (d) monstar and (e) star in **π**-symmetric polarization ellipse orientation field and the corresponding structures in **2π**-symmetric Stokes vortex field (a′) radial (b′) spiral (c′) circulation (d′) node and (e′) saddle. Color bar is **−π/2** to **+π/2** for half-index and **−π** to **+π** for integer index maps.

In addition, the monstar and star patterns (Figure 5.2.1(d)-(e)) in the polarization ellipse orientation field the corresponding patterns in the Stokes vortex field are node and saddle (Figure 5.2.1(d′)-(e′)). These results make us to conclude that, as in Chapter 2 we derived all half-index topological structures from the linear superposition of lemon and star structures. Similarly we can construct all index one topological structures from the linear superposition of radial and saddle structures.

5.3. Topological sphere of index one

The topological flow structures in vector field can be easily represented in the matrix form similar to Equation (5.1.3).

$$\begin{bmatrix} v_x \\ v_y \end{bmatrix} = \begin{bmatrix} M_{11} & M_{12} \\ M_{21} & M_{22} \end{bmatrix} \begin{bmatrix} x \\ y \end{bmatrix} \tag{5.3.1}$$

The flow will take the form of radial or saddle if M will be of the form

$$M_{rad} = \begin{bmatrix} 1 & 0 \\ 0 & 1 \end{bmatrix} \; or \; M_{sad} = \begin{bmatrix} 1 & 0 \\ 0 & -1 \end{bmatrix} \tag{5.3.2}$$

As was pointed out in Section 5.2, by locally rotating each element of radial, we can transform the radial flow to spiral to circulation and vice-versa. This local rotation can be achieved by operating with the rotation matrix:

$$\begin{bmatrix} v_{rad_x} \\ v_{rad_y} \end{bmatrix} = \begin{bmatrix} \cos\alpha & -\sin\alpha \\ \sin\alpha & \cos\alpha \end{bmatrix} \begin{bmatrix} 1 & 0 \\ 0 & 1 \end{bmatrix} \begin{bmatrix} x \\ y \end{bmatrix} \tag{5.3.3}$$

$$\begin{bmatrix} v_{sad_x} \\ v_{sad_y} \end{bmatrix} = \begin{bmatrix} \cos\alpha & -\sin\alpha \\ \sin\alpha & \cos\alpha \end{bmatrix} \begin{bmatrix} 1 & 0 \\ 0 & -1 \end{bmatrix} \begin{bmatrix} x \\ y \end{bmatrix} \tag{5.3.4}$$

Here $\alpha = (0 - 2\pi)$. The Equation (5.3.3) represent pure radial, spiral and circulation for $\alpha = 0(\pi), \pi/4(5\pi/4)$ and $\pi/2(3\pi/2)$ respectively. Action of rotational matrix on saddle will not transform the structures it will only rotate the whole structure. Now consider the linear superposition of Equation (5.3.3) and (5.3.4) with γ as the amplitude factor controlling the amplitudes:

$$\begin{bmatrix} V_x \\ V_y \end{bmatrix} = \begin{bmatrix} \cos(\gamma/2) v_{rad_x} + \sin(\gamma/2)\, v_{sad_x} \\ \cos(\gamma/2) v_{rad_y} + \sin(\gamma/2)\, v_{sad_y} \end{bmatrix} = \begin{bmatrix} F_{11} & F_{12} \\ F_{21} & F_{22} \end{bmatrix} \begin{bmatrix} x \\ y \end{bmatrix} \tag{5.3.5}$$

Here $\mathrm{F}_{11} = 1 + \tan\left(\frac{\gamma}{2}\right)$, $\mathrm{F}_{12} = -\tan(\alpha)\left[1 - \tan\left(\frac{\gamma}{2}\right)\right]$, $\mathrm{F}_{21} = \tan\alpha\left[1 + \tan\left(\frac{\gamma}{2}\right)\right]$ and $F_{22} = 1 - \tan\left(\frac{\gamma}{2}\right)$, where $\gamma = (0 - 180)$. It will represent positive and negative index topological structures for $\gamma < \pi/2$ and $\gamma > \pi/2$ respectively. The possible topological structures in the vector fields can be found if we construct the streamlines by looking for family of solutions of differential equation [12,13]:

$$\frac{dy}{dx} = \frac{V_y}{V_x} = \frac{F_{11}x + F_{12}y}{F_{21}x + F_{22}y} \tag{5.3.6}$$

The (topological structure) solutions of the above differential equation will have four radial lines (node or saddle) if the discriminant $\Delta = (F_{11} - F_{22})^2 + 4F_{12}F_{21} > 0$. Therefore it will be node (or saddle) if $\Delta > 0$ and $\gamma < \frac{\pi}{2} (or > \frac{\pi}{2})$. Figure 5.3.1 shows the numerical solutions plot of number of radial lines which is the 2-D projection of topological sphere of index one.

The salient features of the topological sphere of index one are as follows:

1. It represents the topological sphere of index one with polar coordinate (γ, α) as its longitude and latitude.
2. All the topological structures are found within $\alpha = 0$ to π, after which all topological structures repeat itself but with reversed flow.
3. Along the longitudes and latitudes the structures squeeze or stretch and rotate respectively.
4. The northern hemisphere represents positive index topological structures with unstable radial on the north pole (0,0).
5. The green region represents all possible nodes with four radial lines.
6. The red region belongs to all possible spirals with circular or elliptical unstable structures at $\alpha = \frac{\pi}{2}$ and $\frac{3\pi}{2}$.

7. The unstable spide (**spi**ral-no**de**), intermediate between spiral and node having two radial lines lies on the boundary of green and red zones.
8. The equator represents flow line singular topological structures where the flow direction is undetermined along the line.
9. The southern hemisphere represents all negative index topological structures i.e. all saddle with the symmetric saddle on the south pole $(\pi, 0)$.

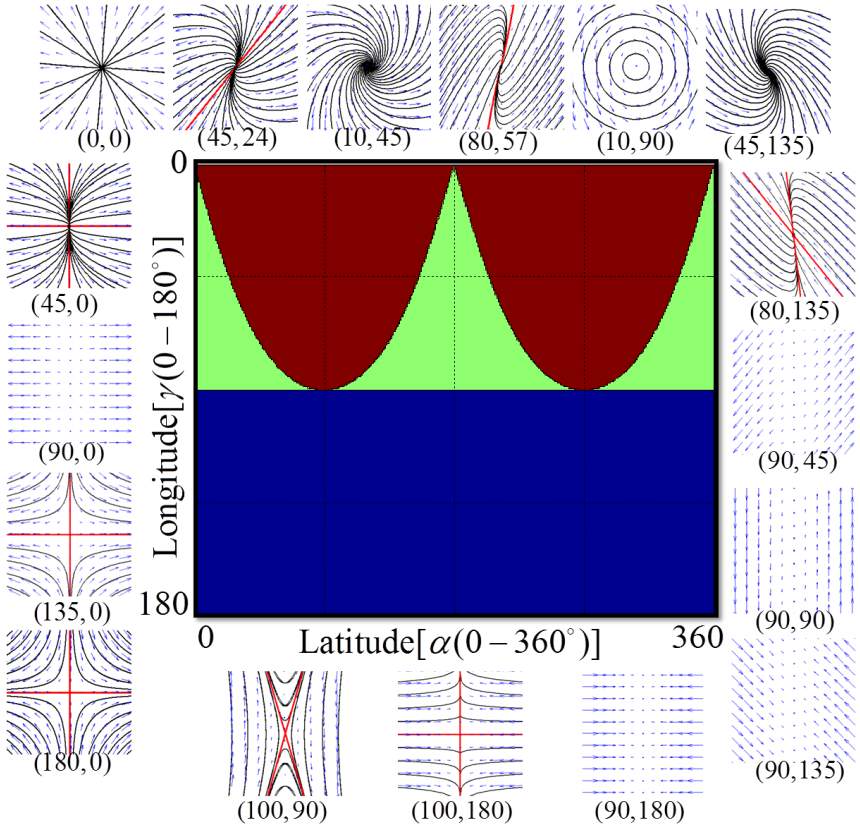

Figure 5.3.1. 2-D projection of the topological sphere of index one. Color representation: node(green), spiral(red) and saddle(blue). Inserts show the topological structures at the respective polar coordinate $(\boldsymbol{\gamma}, \boldsymbol{\alpha})$ with blue arrows showing the flow direction. Spide exists at the boundary between the green and red and circulation or elliptical flow is found at $\boldsymbol{\gamma = \pi/2 \text{ or } 3\pi/2}$. Equator is occupied by flow line singularities. All the topological structures are found within $\boldsymbol{\alpha = 0 - \pi}$ afterwards all the topological structures repeats itself with inverted flow.

5.4. Experimental realization of index one topology

The experimental setup used to generate the topological structures in 2π-symmetric vector fields is shown in Figure 5.4.1. A coaxially aligned Mach-Zender interferometer is used to realize topological structures in three different types of fields: 1. Poynting vector field, 2. Linearly polarized field and 3. Elliptically polarized field. First two are 2π-symmetric vector fields, whereas third is a π-symmetric field. Here we will be presenting only a few special symmetric cases like radial, spiral, circulation and saddle. The node and flow line singular topological structures are realized only in Poynting vector field. This can be extended for the complete realization of the topological space of index one topological sphere.

5.4.1 Poynting vector field

In scalar optical beams the transverse Poynting vector field is directly proportional to the product of the intensity (I) and gradient of the phase (ϕ) given by $S_{x,y} = \frac{1}{k} I_{x,y} \nabla \phi_{x,y}$. Here the phase can be extracted using the Stokes parameters $\phi = arg\ (S_2 + iS_3)$. Therefore we can realize any Poynting vector flow structures by engineering the wavefront [14]. Consider the experimental setup shown in Figure 5.4.1 with $\phi(x, y)$ only in the reflected arm of the interferometer and no quarter-wave plate (Q) at the output. The phase $\phi(x, y)$ is engineered using the cylindrical lens or spherical lens or spiral phase plate or their combinations. The reflected and transmitted beams with engineered and plane phase combine to interfere at the polarizing beam splitter at the interferometer output. The interferometer output now is inhomogeneously polarized due to the superposition of orthogonal linearly polarized beams with engineered and plane wavefronts. Since in our experiments one of the beams has a plane wavefront, the measurement of output polarization using Stokes parameters will directly give the engineered phase structure. We get a radial transverse Poynting vector flow for spherical lens and flow line singular structure for the cylindrical lens shown in Figure 5.4.2(a) and (b). A

combination of spherical and cylindrical lenses in the reflected beam will result in an optical beam whose phase structure takes the form $\phi(x,y) = a(x^2+y^2) + bx^2$, where *a, b* are real numbers. The transverse Poynting vector flow of this beam will be a node if $ab > 0$ i.e., when both the wavefronts are converging or diverging and a saddle if $ab < 0$ i.e., when one wavefront is converging and the other diverging as shown in Figure 5.4.2(d) and (e). The radial Poynting vector flow is a special case of node when $b = 0$. The spiral phase plate in the reflected arm will produce vortex beam with phase $\phi(x,y) = arg\,(x+iy)$ giving us transverse Poynting vector circulation (Figure 5.4.2(c)). A combination of spiral phase plate and spherical lens will form spiral flow structure in transverse Poynting vector. In general we can realize all the index one topological structures in transverse Poynting vector field by considering a phase function of the form $\phi(x,y) = a(x^2+y^2) + bx^2 + c \times arg(x+iy)$, where a, b are real numbers and $c\ (= \pm l)$ is an integer.

5.4.2 Vector beams

The special class of inhomogeneously beam with linear polarization throughout the beam cross section having the cylindrical symmetry is known *cylindrical vector beams*. These beams are formed due to superposition of orthogonal circularly polarized vortex beams of opposite charge:

$$\vec{E}_{VB} = \left((x+ily)\hat{e}_R + e^{i\alpha}(x-ily)\hat{e}_L\right)e^{-\frac{r^2}{2\omega}} \qquad (5.4.1)$$

Here l is the charge of vortex, $\hat{e}_R = \hat{x} - i\hat{y}$ and $\hat{e}_L = \hat{x} + i\hat{y}$ are right and left circular polarization and α is the relative phase difference between the two vortex beams. If $l = +1$ then for $\alpha = 0, \pi/2, \pi$, it will form radial, spiral, azimuthal (circulation) vector beams respectively. For $l = -1$, this will form anti-radial (or hyperbolic or saddle) vector beam.

In order to realize these cylindrical vector beams consider the experimental setup shown in Figure 5.4.1 with $\phi(x,y) = (x+iy)$ (achieved using the spiral phase plate) in the beginning of the interferometer, with a dove prism (DP) in the transmitted arm and a quarter-wave plate with its optical axis making an angle of $\pi/4$ with the horizontal and a half-wave plate

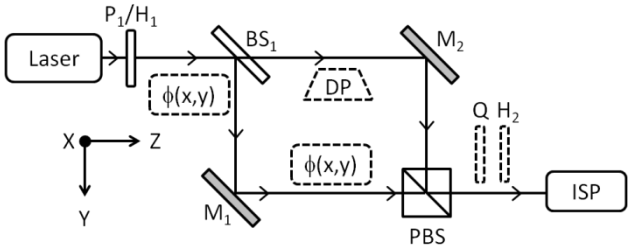

Figure 5.4.1. Experimental setup use to generate topological structures in 2π-symmetric fields. P: Polarizer, H: Half waveplate, BS: Beam splitter, DP: Dove prism, M: Mirror, PBS: Polarizing beam splitter. Q: Quarter waveplate, ISP: imaging stokes polarimeter, $\boldsymbol{\phi}(\boldsymbol{x},\boldsymbol{y})$: phase structure constructed using spherical lens, cylindrical lens, spiral phase plate or their combination.

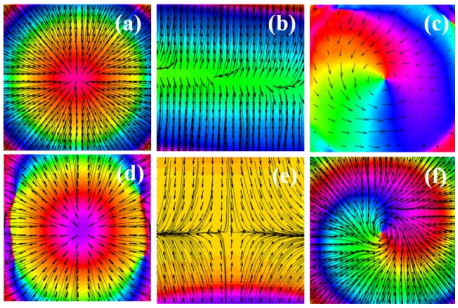

Figure 5.4.2. Experimental results. Topological structures in Poynting vector field superimposed on the color coded phasemap. (a)Radial, (b)flow line singularities, (c)circulation, (d)node, (e)saddle, (f)spiral. Black arrows indicate flow direction. Black lines are streamlines tangent to the local flow directions.

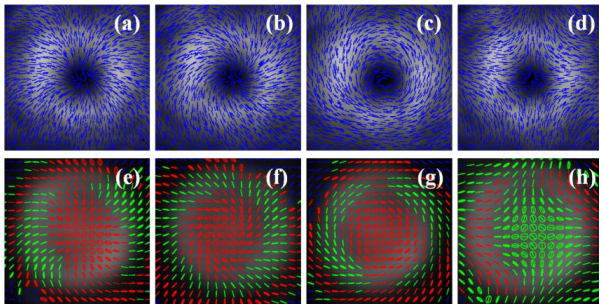

Figure 5.4.3. Experimental results. Topological structures in polarization singularities superposed on the gray scale intensity patterns. Top row: V-singularity patterns in linear polarization. Bottom row: C-singularity patterns in elliptical polarization. (a) and (e) radial, (b) and (f) spiral, (c) and (g) circulation and (h) saddle. Small blue lines are local linear polarization, red and green ellipses represent local right or left elliptical polarization.

at the output. The vortex beam produced by the spiral phase plate is pass through the coaxially aligned Mach-Zender interferometer. In the transmitted arm the dove prism is kept to invert the vortex charge. The output of the polarizing beam splitter (PBS) will be a superposition of orthogonal linearly polarized opposite charge vortex beams, which pass through quarter-wave plate (Q) to makes them orthogonal circular. The half-wave plate at the input (H_1) is used to control the amplitudes and H_2 is used to tune the relative phase between the two vortex beams. The final polarization states are measured using imaging Stokes polarimetry (Appendix B) and the spatially resolved local polarization map superposed on the intensity is constructed as shown in Figure 5.4.3(a)-(d). The small blue lines represent the local linear polarization directions. These polarization maps are structures in linear polarization and are time averaged and so arrow cannot be used as in the Poynting vector structures. We can only say that any instant of time the local electric field direction is along the blue lines. At the centre of the vector beam, the linear polarization is not defined thus there exist a *V-singularity* [15].

5.4.3 Higher-order Poincare beams

Poincare beams are those with all polarization states represented on the Poincare sphere, thus the name [16]. Higher-order Poincare beams can be formed due to linear superposition of orthogonal circularly polarized higher-order vortex and Gaussian beams:.

$$\vec{E}_{PB} = \left[\{x + i\, sgn(l)y\}^{|l|}\hat{e}_R + e^{i\alpha}\hat{e}_L\right]e^{-\frac{r^2}{2\omega}} \tag{5.4.2}$$

where $\boldsymbol{l = \pm 2}$ and $\boldsymbol{sgn}$ is the sign function which takes only the sign of l. Here also the Poincare beams forms radial, spiral, azimuthal (circulation) structures in elliptical polarization for $\boldsymbol{\alpha = 0, \pi/2, \pi}$ respectively.

The experimental realization of the topological structures in Poincare beams is carried out using the setup shown in Figure 5.4.1. Consider only $\phi(x, y)$ (which is vortex beam of charge two produced using spiral phase plate) and Q-H_2 combination. The coaxial superposition of charge two vortex beam and Gaussian beam is carried out in the Mach-Zender interferometer.

The function of quarter-wave plate (Q) is to make them orthogonal circular and H_2 is used to tune the relative phase α. The final output beam polarization is measured using the imaging Stokes polarimetry and the spatially resolved local polarization ellipse map is constructed as shown in Figure 5.4.3(e)-(h). We can clearly see circular polarization at the centre of the beam surrounded by well organized polarization ellipses. At the centre the polarization is circular and therefore ellipse orientation cannot be defined thus is a *C-singularity* [15]. The Complete topological space of topological structures of index one can also be easily realized using Poincare beams.

One important thing to be noted here is that the ellipse field is π-symmetric and therefore the fundamental structures will be half-index lemon, star and monstar and not the radial, spiral, node, saddle etc. of index-one. In the ellipse field index-one structures are unstable and the higher-order structures splits to half-index structures even under small perturbations. As an example, the radial, spiral, node structures will split into two lemon whereas saddle splits into two stars [17]. Even a perfect linear polarization is not possible and therefore the actual linearly polarized vector beams are elliptically polarized vector beams which also have index-one structures as unstable higher-order structures. This implies that the best way to realize index one topological structure is through Poynting vector field.

5.5. Summary

A unified model of all possible symmetric and asymmetric topological structures in 2π-symmetric field is developed by representing them on the surface of the sphere called a topological sphere of index one. The index one fundamental structures are radial, spiral, circulation (elliptic), node, spide and saddle. Out of these radial, spide and circulation are unstable and the rest are stable under perturbation. The topological sphere of index one is constructed by knowing the fact that all possible structures can be constructed from linear superposition of radial and saddle. The experimental

realization of index one topological sphere is performed using transverse Poynting vector field, vector beams and high-order Poincaré beams.

The central idea of this chapter is yet to be published but few results are taken from the publications, Optic Letters 38, 3886-3889 (2013) and Journal of Optical Society of America B, 31, A40-A45 (2014).

5.6. References

1. "Background Imaging of Cosmic Extragalactic Polarization-2," http://www.cfa.harvard.edu/CMB/bicep2/science.html.
2. E. Komatsu, "Matter Adds Twist to Cosmic Microwave Background," Physics **6**, 107 (2013).
3. D. Hanson et.al., "Detection of B-Mode Polarization in the Cosmic Microwave Background with Data from the South Pole Telescope," Phys. Rev. Lett. **111**, 141301 (2013).
4. L. S. Hirst, A. Ossowski, M. Fraser, J. Geng, J. V. Selinger, and R. L. B. Selinger, "Morphology transition in lipid vesicles due to in-plane order and topological defects," Proc. Natl. Acad. Sci. **110**, 3242–3247 (2013).
5. M. B. Nagarajan, P. Coan, M. B. Huber, P. C. Diemoz, and A. Wismüller, "Phase contrast imaging X-ray computed tomography: quantitative characterization of human patellar cartilage matrix with topological and geometrical features," in (2014), Vol. 9038, pp. 903811–903811–8.
6. B. Senyuk, Q. Liu, S. He, R. D. Kamien, R. B. Kusner, T. C. Lubensky, and I. I. Smalyukh, "Topological colloids," Nature **493**, 200–205 (2013).
7. N. Nagaosa and Y. Tokura, "Topological properties and dynamics of magnetic skyrmions," Nat. Nanotechnol. **8**, 899–911 (2013).
8. K. Lou, S.-X. Qian, Z.-C. Ren, C. Tu, Y. Li, and H.-T. Wang, "Femtosecond Laser Processing by Using Patterned Vector Optical Fields," Sci. Rep. **3**, (2013).
9. V. V. Isaeva, N. V. Kasyanov, and E. V. Presnov, "Topological singularities and symmetry breaking in development," Biosystems **109**, 280–298 (2012).

10. M. Tabor, *Chaos and Integrability in Nonlinear Dynamics: An Introduction* (Wiley, 1989).
11. I. Freund, "Poincaré vortices," Opt. Lett. **26**, 1996–1998 (2001).
12. L. R. Ford, *Differential Equations*, 2nd edition (McGraw-Hill Inc.,US, 1955).
13. I. Freund, "Optical Möbius strips in three dimensional ellipse fields: II. Lines of linear polarization," Opt. Commun. **283**, 16–28 (2010).
14. V. Kumar and N. K. Viswanathan, "Topological structures in the Poynting vector field: an experimental realization," Opt. Lett. **38**, 3886–3889 (2013).
15. I. Freund, "Polarization singularity indices in Gaussian laser beams," Opt. Commun. **201**, 251–270 (2002).
16. A. M. Beckley, T. G. Brown, and M. A. Alonso, "Full Poincare beams," Opt. Express **18**, 10777–10785 (2010).
17. T. Delmarcelle and L. Hesselink, "The topology of symmetric, second-order tensor fields," in *Proc. IEEE Conference on Visualization, 1994.* (1994), pp. 140–147.

Chapter 6

Dynamical properties of topological structured beam-fields

Contents

Vijay Kumar under the supervision of Prof. Nirmal K. Viswanathan
School of Physics, University of Hyderabad, India

Chapter

6

Dynamical properties of topological structured beam-fields

"Nobody before Poynting seems to have thought of tracing the flux of energy in a medium elastically transmitting it, and where the whole process is therefore exposed to view… I take it this idea is Poynting's main contribution, and it clarified many things..."

- Sir Joseph Larmor on Poynting Theorem, Cambridge, 1915.

Once J. H. Poynting established the fact that electromagnetic fields posses angular momentum and Poynting vector represents the transfer of energy thereafter these physical quantities have becomes the fundamental quantities of electromagnetic fields. Thus, the two revolutionary ideas of "Poynting vector" and "Angular momentum" of light changed the way we understand electromagnetic fields. Currently these are extensively used for imparting mechanical motion to microscopic particle and for micro/nano manipulations.

In this chapter we explore the orbital, spin and total Poynting vector densities in fundamental polarization topological structures such as lemon, star, dipole and C-line singularities. We will see that polarization topological structures can be used to engineer the Poynting vector densities. We had also explored two physical manifestations: the transverse energy flow and polarization topological structure (lemon) rotation of the topologically structured beam when focused using a spherical lens. It was found that these two physical manifestations are due to the Gouy phase.

TOPOLOGICAL OPTICS: STRUCTURED BEAM-FIELDS

6.1. Introduction

In 1884, in his well known paper on "On the transfer of energy in the electromagnetic field" [1], J. H. Poynting wrote *"The aim of this paper is to prove that there is a general law for the transfer of energy, according to which it moves at any point perpendicularly to the plane containing the lines of electric and magnetic force, and that the amount crossing unit of area per second of this plane is equal to the product of the two forces multiplied by the sine of the angle between them divided by* 4π*, while the direction of the flow of energy is that in which a right-handed screw would move if turned round from the positive direction of the electromotive to the positive direction of the magnetic intensity"*. Now, this general law for the transfer of energy is known as "Poynting theorem" and the physical quantity "Poynting vector" represents the transfer of energy in electromagnetic fields. In another paper by J. H. Poynting in 1909 on "The wave motion of a revolving shaft, and a suggestion as to the angular momentum in a beam of circularly polarised light" [2], he wrote, *"The analogy between circularly polarised light and the mechanical model suggests that a similar relation between torque and energy may hold in a beam of such light incident normally on an absorbing surface. If so, a beam of wave-length* λ *containing energy* E *per unit volume will give up angular momentum* $E\lambda/2\pi$ *per second per unit area. But in the case of light wave* $E = P$*, where* P *is the pressure exerted. We may therefore put the angular momentum delivered to unit area per second as* $P\lambda/2\pi$*"*. This proves the existence of "angular momentum" of light which was experimentally confirmed by Beth in 1936 [3]. Thus, the two revolutionary ideas of "Poynting vector" and "Angular momentum of light" changed the way we look at electromagnetic fields.

In this chapter the orbital, spin and the Poynting vector densities of the fundamental polarization topological structures such as lemon, star, dipole and C-line singularities are explored. In addition, their physical manifestations such as transverse energy flow and rotation of polarization topological structures are also studied.

6.2. Poynting vector in topologically structured beams

Poynting vector is one of the most essential properties of the electromagnetic fields. In this section we have theoretically and experimentally realize the Poynting vector of the fundamental structures: lemon, star, dipole and C-line singularity structures of the topologically structured electromagnetic fields. Under paraxial-approximation the Poynting vector density of the generalized electromagnetic field can be decomposed into orbital ($\vec{P}_o$) and spin ($\vec{P}_s$) parts [4,5].

$$\vec{P}_o = \frac{1}{k}\left(I_i \nabla\varphi_i + I_j \nabla\varphi_j\right) \tag{6.2.1a}$$

$$\vec{P}_s = -\frac{1}{2k}[\vec{e}_z \times \nabla S_3] \tag{6.2.1b}$$

Here $k = 2\pi/\lambda$ is the wave number, $i, j = x, y$ coordinates, I are the intensities and φ are the phases. Under the special cases of complex fields formed due to superposition of orthogonally polarized wave field components, the Poynting vector densities can be written as the sum of two components in the circular ($\pm$) or Cartesian (x, y) basis:

$$\vec{P}_{o(s)} = \vec{P}_{+o(s)} + \vec{P}_{-o(s)} = \vec{P}_{xo(s)} + \vec{P}_{yo(s)} \tag{6.2.2a}$$

$$\vec{P} = \vec{P}_o + \vec{P}_s \tag{6.2.2b}$$

Now consider the optical beam-fields of the forms [6]

$$\vec{E} = E_1\hat{e}_1 + e^{i\varphi}E_2\hat{e}_2 \tag{6.2.3a}$$

$$E_1 = a[x + sign(l_1)iy]^{|l_1|}e^{-\frac{r^2}{2w_0}} \tag{6.2.3b}$$

$$E_2 = b[x + sign(l_2)iy]^{|l_2|}e^{-\frac{r^2}{2w_0}} \tag{6.2.3c}$$

Here $E_1$and E_2 are the complex vortex beam amplitudes with charges l_1 and l_2 respectively with a relative phase of φ. ($\hat{e}_1, \hat{e}_2$) are the orthonormal basis sets. We consider all the three possible basis sets: (1) circular basis set ($\hat{e}_+ = \hat{x} + i\hat{y}, \hat{e}_- = \hat{x} - i\hat{y}$), (2) horizontal and vertical basis set ($\hat{e}_H = \hat{x}, \hat{e}_V = \hat{y}$) and (3) diagonal and anti-diagonal basis set ($\hat{e}_D = \hat{x} + \hat{y}, \hat{e}_A = -\hat{x} + \hat{y}$); where $\hat{x}, \hat{y}$ are the unit vectors along the x and y-directions.

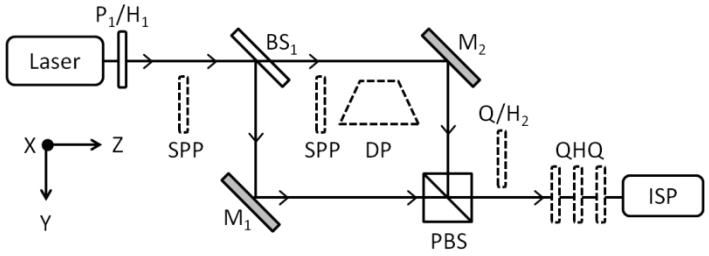

Figure 6.2.1. Experimental setup for realizing complex optical beam fields. P: polarizer; H:half-wave plate; SPP: spiral phase plate; BS: beam-splitter ; M: mirror; DP: Dove prism; PBS: polarization beam-splitter; Q: quarter-wave plate; ISP: imaging Stokes polarimeter.

The above mention optical beam-fields can be easily realized using a coaxially aligned Mach-Zender interferometer as shown in Figure 6.2.1. The spiral-phase plate (SPP) and SPP + DP (Dove prism) combination is kept either outside of the interferometer or inside it to realize the desired complex beam-fields. The use of quarter- or half-wave plate at the output of the interferometer is to work in either circular or desire linear basis. The quarter-half-quarter (QHQ) wave plates combination is used to tune the relative phase between the superposed beams. The standard measurements of imaging Stokes polarimetry (ISP) is carried out for the polarization measurement of the resultant output beam-fields from which all the desired quantities are constructed (Appendix B).

6.2.1 Poynting vector in lemon and star patterned beams

In phase ($\varphi = 0$) superposition of orthogonally polarized Gaussian ($l_1 = 0$) and vortex ($l_2 = \pm 1$) beams in circular basis ($\hat{e}_1 = \hat{e}_+, \hat{e}_2 = \hat{e}_-$) will form a lemon (star) polarization topological structure in the beam cross-section for $l_2 = +1\,(-1)$. For the above-mentioned two cases of beams with lemon and star topological patterns, the orbital, spin and total Poynting vector density plots are theoretically calculated and constructed from Equation 6.2.1-6.2.2 as shown in Figure 6.2.2 and Figure 6.2.3. For the experimental construction, the phase and S_3 are measured using Stokes polarimetry. The orbital and spin component of the Poynting vector has a

singularity at the origin, forming a circulation around it. The orbital flows are centered on the vortex core in both the cases but are in opposite directions signifying the vortex charges which arise due to the vortex components only. The spin flow on the other hand remains the same as the handedness of the circular polarization of the interfering beams remain the same. In the spin flow we see a circulation centered on the C-point and as we move away, a contour of zero flow which separates the opposite flow appear which is formed due to the change in the sign of the gradient of third Stokes parameter S_3. This sign change occurs due to either the change in the polarization handedness or the amplitude change [7]. In the above case it is cumulative effect of both the reasons. The total Poynting vector density is the sum of orbital and spins flow densities. For lemon pattern we find that the zero flow contour size enlarges whereas for star pattern it reduces because of the addition or subtraction of the orbital and spin flows respectively. Thus, in complex vector fields there is a possibility of local enhancement in the total Poynting vector density and the angular momentum [8] which can be useful in practical applications such as optical trapping and micro- / nano-manipulation.

6.2.2 Poynting vector in dipole patterned beams

Now we consider one of the above situations in linear basis i.e., in phase superposition of orthogonal linearly polarized Gaussian and vortex beams. If we choose the basis set as ($\hat{e}_1 = \hat{e}_H, \hat{e}_2 = \hat{e}_V$) or ($\hat{e}_1 = \hat{e}_D, \hat{e}_2 = \hat{e}_A$) we find polarization topological dipole which is a combination of star and lemon pattern in the beam across-section. The Poynting vector densities of the above dipoles remain the same. The orbital part of the Poynting vector of the above dipoles will be independent of the polarization basis as this contribution arises only from the phase structure of the component vortex field and hence depend only on its phase gradient which will be the same as for that of the lemon or star case. The spin part of the Poynting vector will have opposite circulations centered on the two C-points of the dipole, resulting in maximum

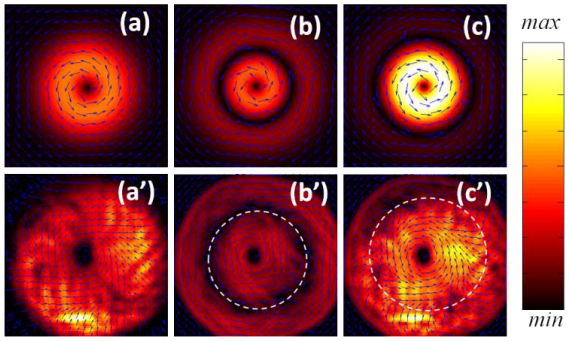

Figure 6.2.2. Poynting vector densities of lemon patterned beam-field. Simulated (a) orbital, (b) spin and (c) total Poynting vector densities. (a′)-(c′) are the corresponding plots from experimental measurements.

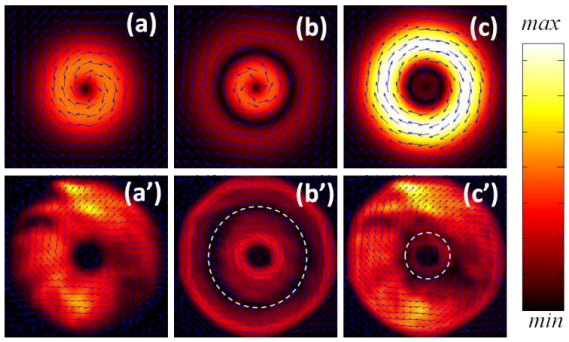

Figure 6.2.3. Poynting vector densities of star patterned beam-field. Simulated (a) orbital, (b) spin and (c) total Poynting vector densities. (a′)-(c′) are the corresponding plots from experimental measurements.

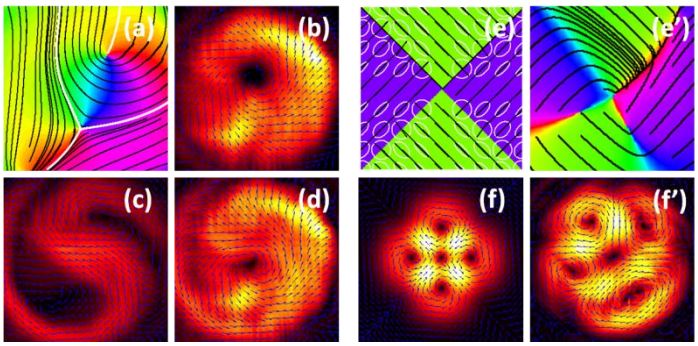

Figure 6.2.4. Poynting vector densities of (a) dipole and (e)-(e′) C-line singularity patterned beam-field. Experimental (b) orbital, (c) spin and(d) total Poynting vector of dipole. (e)-(f) are simulated C-line singularity pattern and its corresponding spin Poynting vector density, (e′)-(f′) are the corresponding plots from experimental measurements.

spin flow between the two C-points. The total Poynting vector density of the whole beam is the sum of these two contributions. An experimentally generated topological dipole pattern and its corresponding Poynting vector densities are shown in Figure 6.2.4(a)-(d).

6.2.3 Poynting vector in C-line singularity patterned beam

The linear superposition of opposite charge vortex beams in circular basis will form vector beams with zero total as well as local Poynting vector and angular momentum densities. In the linear basis however, this will give a beam with zero total and local orbital Poynting vector densities but zero total and non-zero local spin Poynting vector densities. Consider only the case of in-phase linear superposition of orthogonal linearly polarized ($\hat{e}_1 = \hat{e}_H, \hat{e}_2 = \hat{e}_V$) vortex beams ($l_1 = +1, l_2 = -1$) as shown in Figure 6.2.4(e)-(e'). We see that the C-lines and L-lines (locus of circular or linear polarization respectively) cross at right angle to each other forming a four lobe pattern of opposite circular polarization. The spin Poynting vector density for this case calculated using Equation 6.2.1(b) is shown in Figure 6.2.4(f)-(f'). This clearly shows four circulations centered on the C-lines, forming a saddle at the origin. The deviation of the experimental measurements from the simulated plots is due to non-zero relative phase between the interfering beams and the unavoidable beam divergence. This example of a beam combination will be very much useful in the study of orbital motion contribution from the spin only [7,9].

6.3. Manifestations of topologically structured beams

6.3.1 Transverse energy flow in isotropic vortex

The transverse energy flow (TEF) in a beam is due to the transverse component of the Poynting vector and beams with transverse component of Poynting vector posses orbital angular momentum (OAM). Recently it was shown that the orbital angular momentum of a paraxial light beam is related

to the rotational features of the instantaneous optical-frequency oscillation pattern within the beam cross section which corresponds to the transverse energy flow in the experimentally observable time-averaged field [12,13]. The TEF therefore, is a useful physical manifestation for observing OAM and is a more practical approach to understand the complex nature of wave fields. In this section we will experimentally prove that the TEF in topologically structured beams having vector character is also principally governed by the gradient of phase (of component fields) as was shown in the past for scalar beams [14–16].

As we can see from Equation 6.2.1(a), transverse the Poynting vector or the TEF is directly proportional to the phase gradient. In the past also it was shown that for isotropic optical vortex with constant phase gradient in the azimuth direction, the total rotation (θ) of the TEF from the beam waist to a position z is directly proportional to the product of vortex charge (l) and Gouy phase: $\theta = \frac{l}{2}\left(\frac{\omega(z)}{r(z)}\right)^2 \tan^{-1}\left(\frac{z}{z_r}\right)$ [17]. Here $\omega(z)$ and $r(z)$ are the beam size and a point on the beam at position z, and z_r is the Rayleigh range. We adopt this approach and track the TEF acros the beam cross-section within the Rayleigh range.

Now consider topologically structured beam with desired characteristics, generated using a two-mode optical fiber (TMF) as shown in Figure 6.3.1. Launching circularly polarized light ($\sigma = +1$) and adjusting the launch conditions of the TMF we get best possible isotropic vortex beam at the fiber output with asymmetric intensity around the circular vortex core (Figure 6.3.2(a)). Without disturbing the launch conditions but changing the handedness of the input beam polarization to $\sigma = -1$ we get an isotropic vortex (Figure 6.3.1(d)) with opposite charge verified by measuring the interference patterns (Figure 6.3.1(b) and (e)). The Stokes parameters of the output beam are measured from which spatially-resolved polarization map is constructed as shown in Figure 6.3.1(c) and (f). Now the output collimated beam from the TMF is focused by the lens L_3 ($f = 17.5cm$) and taking the focal point to be at $z = 0$ the angle of rotation (θ) of the maximum intensity point (MIP) of the focused beam is plotted as a function of the propagation

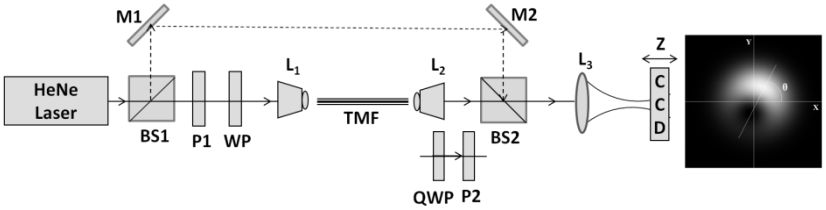

Figure 6.3.1. Experimental setup. BS: Beam splitter; M1, M2: Mirrors; P1, P2: Polarizers; WP: Wave plate; QWP: quarter wave plate; L1, L2: Microscope objectives; L3: biconvex lens; TMF: two-mode fiber. Inset shows the image in the CCD.

distance z. This measurement shows that the transverse energy flow is in opposite directions for $l = +1$ and -1. A careful look at the measured fiber output polarization map shown in Figure 6.2.3(c) for input polarization $\sigma = \pm 1$, the output mode combination can be written as a linear superposition of circularly polarized modes [18,19]: $CP_{11}^{O+} + ilCP_{11}^{e-}$ where $CP_{11}^{O+} = \left(HE_{21}^{O} + TE_{01}\right) - i(HE_{21}^{e} - TM_{01})$ and $CP_{11}^{e-} = (HE_{21}^{e} + TM_{01}) - i(HE_{21}^{o} - TE_{01})$. If $l = +1$, $CP_{11}^{O+} + iCP_{11}^{e-} = 2(HE_{21}^{o} + iTM_{01})$ or if $l = -1$, $CP_{11}^{O+} - iCP_{11}^{e-} = 2(TE_{01} - iHE_{21}^{e})$. This implies that for the particular off-axis launch condition and input polarization $\sigma = +1(-1)$, the HE_{21}^{o} and TM_{01} (TE_{01} and HE_{21}^{e}) Eigen vector modes are excited in the fiber, resulting the vortex charge of $l = \pm 1$ at the fiber output. The second and fourth row of the Figure 6.3.2 shows the simulated polarization map as expected for the linear combination of CP modes as mentioned above. The deviation in polarization ellipticity and in the orientation of the measured modes at the fiber output is due to the fiber birefringence and the optical Magnus effect [20] resulting due to the spin-orbit interaction experienced by the off-axis Gaussian beam. This example of topologically structured beam having vector character proves that that major factor controlling the TEF is still the vortex charge. But in the case of vector field we have to consider the gradient of phase of the component field.

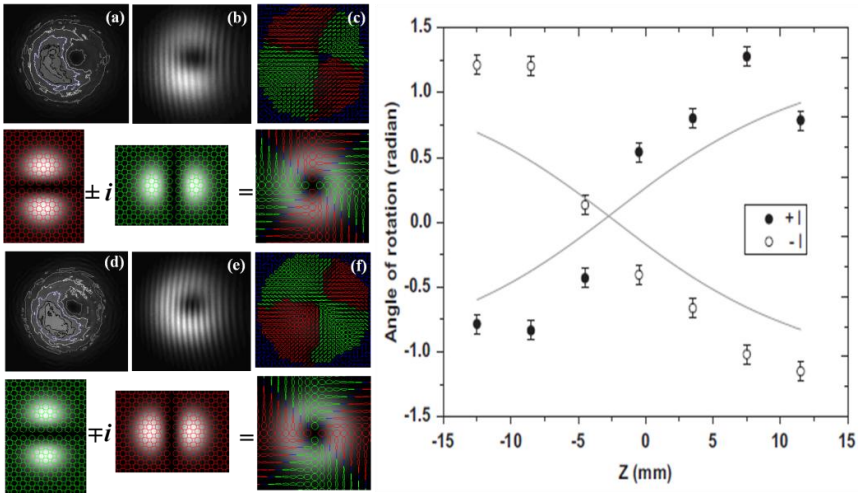

Figure 6.3.2. Experimental results. (a) and (d) beam intensity with contours, (b) and (e) are the interference patterns for fiber output with corresponding polarization maps (c) and (f) for $\boldsymbol{\sigma} = \pm\mathbf{1}$ input polarization. 2nd and 3rd row shows the simulated polarization map of the CP mode combinations. Red (green) corresponds to right (left) circular polarization. Graph shows the angle of rotation of the maximum intensity point with propagation distance and solid lines shows the fit to Gouy phase relation.

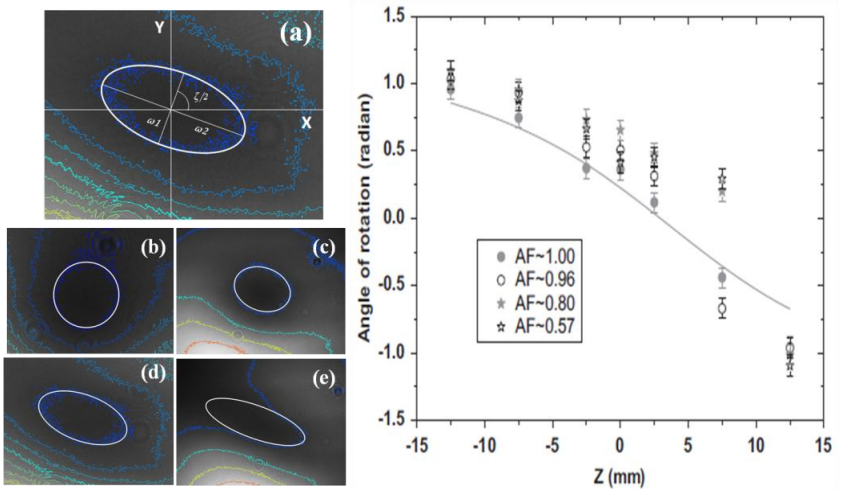

Figure 6.3.3. Experimental results. (a) Morphology parameters of the anisotropic optical vortex core: ω_1 and ω_2 are the semi-minor and semi-major axes of the ellipse core and $\boldsymbol{\zeta}$ is the angle of orientation, which is twice the angle by which the ellipse is oriented with respect to the *x*-axis. (b)-(e) are the intensity contour around the vortex core for anisotropic factor (AF) 1, 0.96, 0.80, 0.57 respectively and $\boldsymbol{\zeta} = \mathbf{140}^{\circ}$. Graph shows the angle of rotation of the maximum intensity point with propagation distance and the solid line is a fit to the Gouy phase relation.

6.3.2 Transverse energy flow in anisotropic vortex

Anisotropic optical vortices (AVs) having an elliptical core appearance can be considered more generic then isotropic vortices (IVs). The AVs can be parameterized and have inhomogeneous angular momentum density [21–24]. If we assume the AVs as a combination of two oppositely charged IVs then it is characterized by an anisotropy factor (AF) $cos(\psi) = 2(\frac{\omega_1}{\omega_2} + \frac{\omega_2}{\omega_1})^{-1}$ where, ω_1 and ω_2 are the semi-minor and semi-major axes of equal intensity contour around the vortex core and the angle of orientation (ζ) which is twice the angle by which the ellipse of equal intensity is oriented with respect to the fixed coordinate system as shown in the Figure 6.3.3(a). We have adopted the scheme of reference [24] for the morphology of AVs. The TEF of the AV beams with asymmetric vortex core and intensity profile as shown in Figure 6.3.3(b)-(e) is measured as before by tracking the maximum intensity point (MIP) of the beam. We use the same experimental setup as in Figure 6.3.1. Now we keep a half-wave plate (HWP) at 45° at the fiber input. The launching condition is adjusted to get an isotropic vortex beam at fiber output with $l = -1$. The IV beam generated pass through lens L_3 of focal length 17.5 *cm* as before and the beam intensity through the Rayleigh range is scanned by CCD camera. Without disturbing the launching conditions the HWP is rotated in steps of five degrees and for every value of the HWP orientation the beam intensities in the Rayleigh range of the lens are recorded. We observe that the vortex core starts losing its symmetry signifying an increase in anisotropy due to increase of weighting coefficient of the $l = +1$ mode in the fiber. The AF and the angle of orientation (θ) are calculated from the intensity contour [24] around the vortex core shown in Figure 6.3.3(b)-(e) and is found to vary from AF ~1 to 0.57 with a fixed $\zeta = 140^{\circ}$ as HWP is rotated from 45° to 30°.

Taking the focal point to be at $z = 0$, the angle of rotation of the maximum intensity point (MIP) in the beam is plotted as a function of the propagation distance (z) as shown in graph Figure 6.3.3. The rotation of MIP of the beam (for AF~1) clearly demonstrates that the transverse energy

circulation decreases as we increase the amount of anisotropy of the beam by rotating the HWP angle to 30^{o}. The measurements can be understood by considering the transverse Poynting vector distribution across the beam profile. Since the Poynting vector is proportional to the phase gradient which for an IV is constant in the azimuthal direction resulting in the TEF following the standard Gouy phase relation. For the anisotropic vortex due to the nonlinear variation of phase profile in the azimuthal direction, the phase gradient and the Poynting vector are maximum near the anisotropic (major) axis and minimum perpendicular to it. Therefore, for the beam with $AF = 0.57$, first the MIP rotates slowly as it reaches near the anisotropic axis where it rotates fastest which is reflected as a sudden jump in the graph Figure 6.3.3. Thus, we have demonstrated that the TEF is directly proportional to the gradient of phase of the component vortex field and is maximum along the anisotropic axis and minimum perpendicular to it. The above two examples prove that TEF is principally governed by the phase gradient of the component fields.

6.3.3 Polarization topological structure rotation

In general, the state of polarization reamins constant under paraxial focusing. But in polarization topological structured beams, the manifestations of the Gouy phase leads to the rotation and evolution of the topological structures. Consider the experimental setup shown in Figure 6.3.1 fiber length 37.4 *cm*. We launch circularly polarized light into the fiber and by adjusting the launch conditions, orthogonal circular polarized Gaussian and vortex modes are excited simultaneously to get the lemon structure at the fiber output as explained in Chapter 2. This lemon pattern is then passed through a spherical lens of focal length $f = 40cm$ and the polarization characteristics along the Rayleigh range is measured using Stokes polarimetry. We observed the rotation of the lemon pattern as it propagates through the lens focus due to the modal dependent Gouy phase$\zeta(z) = (l + 2m + 1)\tan^2(z/z_r)$ [11] as ploted in the Figure 6.3.4. We know from Chapter 2 that if we vary the phase

difference between the Gaussian and vortex modes the orientation of the lemon patterns changes and the Gouy phase depends on the order of the mode. Therefore as the lemon pattern passes through the lens, the Gaussian and vortex beams accquire different amount of Gouy phase leading to an increase in the relative phase difference which makes the lemon pattern to rotate. Recently, the evolution of the higher-order polarization topological structures are also reported as they pass through the lens [25] and it was shown that the radial polarization structure transforms to spiral and to azimuthal due to increase in the relative phase between the constituents modes arises due to the modal dependent Gouy phase.

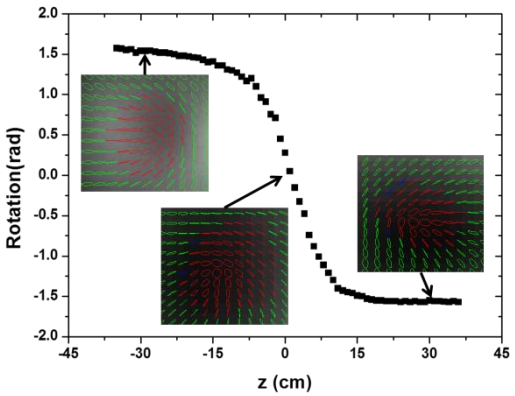

Figure 6.3.4. Rotation of the polarization topological structure (lemon) as it propagates through the lens focus ($\boldsymbol{f = 40cm}$). Inserts show the structure at the respective positions.

6.4. Summary

In this chapter we studied the Poynting vector densities in the fundamental polarization structures: lemon, star, dipole and C-line singularities. The orbital part of the Poynting vector density is directly proportional to the phase gradient whereas spin part of the Poynting vector density depends on the gradient of the third Stokes parameter (S_3). Since these structures are formed as a superposition of scalar beams the orbital part of the Poynting vector density is the sum of the orbital densities of the constituent components and the spin part of the Poynting vector density is

proportional to the gradient of the third Stokes parameter of the resultant polarization topological structure. These fundamental polarization structures may be used to engineer the total Poynting vector density of the beam. We also explored the transverse energy flow in isotropic and anisotropic optical vortices. We found that the TEF is principally governed by the phase gradient of component fields. We also studied the propagation of polarization topological structure as it pass through the lens focus and found that it rotates due to modal dependent Gouy phase.

This chapter is based on the publications, Optic Communication 285, 4866–4873 (2012); Optic Letters. 37, 2667–2669 (2012) and Journal of Optical Society of America B, 31, A40-A45 (2014).

6.5. References

1. J. H. Poynting, "On the Transfer of Energy in the Electromagnetic Field," Philos. Trans. R. Soc. Lond. **175**, 343–361 (1884).
2. J. H. Poynting, "The Wave Motion of a Revolving Shaft, and a Suggestion as to the Angular Momentum in a Beam of Circularly Polarised Light," Proc. R. Soc. Lond. A **82**, 560–567 (1909).
3. R. A. Beth, "Mechanical Detection and Measurement of the Angular Momentum of Light," Phys. Rev. **50**, 115–125 (1936).
4. A. Y. Bekshaev and M. S. Soskin, "Transverse energy flows in vectorial fields of paraxial beams with singularities," Opt. Commun. **271**, 332–348 (2007).
5. A. Bekshaev, K. Y. Bliokh, and M. Soskin, "Internal flows and energy circulation in light beams," J. Opt. **13**, 053001 (2011).
6. V. Kumar and N. K. Viswanathan, "Topological structures in vector-vortex beam fields," J. Opt. Soc. Am. B **31**, A40 (2014).
7. J. P. Torres and L. Torner, *Twisted Photons* (Wiley-VCH, 2011).
8. R. Zambrini and S. M. Barnett, "Angular momentum of multimode and polarization patterns," Opt. Express **15**, 15214–15227 (2007).

9. O. V. Angelsky, A. Y. Bekshaev, P. P. Maksimyak, A. P. Maksimyak, S. G. Hanson, and C. Y. Zenkova, "Orbital rotation without orbital angular momentum: mechanical action of the spin part of the internal energy flow in light beams," Opt. Express **20**, 3563–3571 (2012).
10. V. Kumar, V. V. G. Krishna Inavalli, and N. K. Viswanathan, "Dynamic evolution of transverse energy flow in focused asymmetric optical vector-vortex beams," Opt. Commun. **285**, 4866–4873 (2012).
11. G. M. Philip, V. Kumar, G. Milione, and N. K. Viswanathan, "Manifestation of the Gouy phase in vector-vortex beams," Opt. Lett. **37**, 2667–2669 (2012).
12. A. Y. Bekshaev, "Transverse rotation of the instantaneous field distribution and the orbital angular momentum of a light beam," J. Opt. Pure Appl. Opt. **11**, 094004 (2009).
13. A. Y. Bekshaev, "Internal energy flows and instantaneous field of a monochromatic paraxial light beam," Appl. Opt. **51**, C13–C16 (2012).
14. J. Arlt, "Handedness and azimuthal energy flow of optical vortex beams," J. Mod. Opt. **50**, 1573–1580 (2003).
15. J. Hamazaki, Y. Mineta, K. Oka, and R. Morita, "Direct observation of Gouy phase shift in a propagating optical vortex," Opt. Express **14**, 8382–8392 (2006).
16. S. M. Baumann, D. M. Kalb, L. H. MacMillan, and E. J. Galvez, "Propagation dynamics of optical vortices due to Gouy phase," Opt. Express **17**, 9818–9827 (2009).
17. M. J. Padgett and L. Allen, "The Poynting vector in Laguerre-Gaussian laser modes," Opt. Commun. **121**, 36–40 (1995).
18. A. V. Volyar and T. A. Fadeeva, "Optics of Singularities of the Field of a Low-Mode Fiber:I. Circular Disclinations," Opt. Spectrosc. **85**, 264–271 (1998).
19. A. V. Volyar and T. A. Fadeeva, "Optics of Singularities of a Low-Mode Fiber: II. Optical Vortices," Opt. Spectrosc. **85**, 272–280 (1998).
20. A. V. Dooghin, N. D. Kundikova, V. S. Liberman, and B. Y. Zel'dovich, "Optical Magnus effect," Phys. Rev. A **45**, 8204–8208 (1992).

21. Y. Y. Schechner and J. Shamir, "Parameterization and orbital angular momentum of anisotropic dislocations," J. Opt. Soc. Am. A **13**, 967–973 (1996).
22. I. Freund and V. Freilikher, "Parameterization of anisotropic vortices," J. Opt. Soc. Am. A **14**, 1902–1910 (1997).
23. F. S. Roux, "Distribution of angular momentum and vortex morphology in optical beams," Opt. Commun. **242**, 45–55 (2004).
24. A. Y. Bekshaev, M. V. Vasnetsov, and M. S. Soskin, "Description of the morphology of optical vortices using the orbital angular momentum and its components," Opt. Spectrosc. **100**, 910–915 (2006).
25. F. Cardano, E. Karimi, L. Marrucci, C. de Lisio, and E. Santamato, "Generation and dynamics of optical beams with polarization singularities," Opt. Express **21**, 8815–8820 (2013).

Concluding remarks

Light got its well-established electromagnetic structure, after continuous evolution of more than 2000 years from the times of Plato (423-347 BC) to Maxwell's era (1831–1879 AD). But structuring and manipulating light upto the desired extent and to explore the true nature of light is still an area of current research interest. This is clearly evident from the recent trend of conferences such as: *International conference on Correlation Optics* [1] (1993, 1995, 1997, 1999, 2001, 2003, 2005 2007, 2009, 2011; SPIE Proc. Vols. 2108, 2647, 3317, 3904, 4607, 5477, 6254, 7008, 7388, 8338, respectively), *International conferences on Singular optics* [2] (1997, 2000; SPIE Proc. Vols. 3487, 4403 respectively and 2003, 2008, 2012; J. Opt. Vol.6, No.5, Vol. 11, No.9, Vol. 15, No. 4 respectively), *Conferences on Complex light and optical forces* [3] (2007, 2008, 2009, 2010, 2011, 2012, 2013, 2014; SPIE Proc. Vols. 6483, 6905, 7227, 7613, 7950, 8274, 8637, 8999 respectively). In addition, the biennial workshop on Singular optics at International Centre of Theoretical Physics (ICTP) Trieste, Italy [4,5] is also attracts many young minds to participate and contribute to this area of research. Moreover, several special issues of various journals: *Optical angular momentum* in Journal of Optics (Vol. 13, No. 6, 2011), *Correlation optics* in Applied Optics (vol. 51, Iss. 10, 2012 and vol. 53, Iss. 10, 2014), *Structured light interactions* in JOSA-B (vol. 31, Iss.6, 2014), monographs [6–9] and books [10–15] reflect the fact that structured light and light manipulation is one of the emerging areas of the optics research.

This thesis is a step forward in that direction, towards achieving optical field engineering using singularities and its associated topological structures. The central idea of the thesis is to engineer the amplitude, phase and polarization aspects of optical beam fields using the universal fundamental building block topological structures such as lemon, monstar, star, spiral, node, saddle etc. and to study its manifestations and some physical properties.

Recent experimental confirmation of the "Big-Bang" theory and the detection of dark matter following the topological approach to light [16–19] is an example of the potential of the *Topological Optics*. Moreover, optics can be used as a platform for mimicking and gaining a better understanding of other physical systems [20]. Topologically structured beam-fields promises vast number of future applications and fundamental studies ranging from optical tweezers [21,22], material processing [23], nano structure formation [24], biological studies [25–28], manipulation of optical angular momentum [29–31], plasmonic field engineering [32–34], polarization imaging [28,35], superdense information coding [36], quantum information [37,38], structured light-matter interaction [39] etc.

In addition to the amplitude, phase and polarization, *Coherence* also plays a vital role in determining the physical properties of light fields [40]. Recent studies have shown that optical current and orbital angular momentum is highly dependent on the coherence of the optical beams [41,42]. The obvious future direction is to explore the topological aspects of partially coherent optical fields [43–46] and unify with the present study to get the complete picture of topological optics for the better understanding of light manipulation. The alternate direction would be to understand the quantum mechanical aspect of topologically structured optical field which will help in unravelling the principles of quantum mechanics [47].

References

1. "The 11th International Conference on Correlation Optics 2013," http://www.itf.cv.ua/corropt13/.
2. "6th International Conference on Singular Optics 2014," http://singular-optics.org/.
3. "Conference on Complex Light and Optical Forces IX 2015," http://spie.org/PWO/conferencedetails/complex-light-and-optical-forces.
4. "Workshop on Singular Optics and its Applications to Modern Physics 2011," http://cdsagenda5.ictp.it/full_display.php?ida=a10144.

5. "International Workshop on Singularities and Topological Structures of Light 2013," http://cdsagenda5.ictp.it/full_display.php?email=0&ida=a12190.
6. M. V. Berry and C. Upstill, "Catastrophe Optics: Morphologies of Caustics and Their Diffraction Patterns," in *Progress in Optics* (Elsevier, 1980), Vol. 18, pp. 257–346.
7. L. Allen, M. J. Padgett, and M. Babiker, "The Orbital Angular Momentum of Light," in *Progress in Optics* (Elsevier, 1999), Vol. 39, pp. 291–372.
8. M. S. Soskin and M. V. Vasnetsov, "Singular optics," in *Progress in Optics* (Elsevier, 2001), Vol. 42, pp. 219–276.
9. M. R. Dennis, K. O'Holleran, and M. J. Padgett, "Singular Optics: Optical Vortices and Polarization Singularities," in *Progress in Optics* (Elsevier, 2009), Vol. 53, pp. 293–363.
10. J. F. Nye, *Natural Focusing and Fine Structure of Light* (Institute of Physics Pub., 1999).
11. L. Allen, S. M. Barnett, and M. J. Padgett, *Optical Angular Momentum* (Institute of Physics Pub., 2003).
12. O. V. Angelsky, ed., *Optical Correlation Techniques and Applications* (SPIE, 2007).
13. D. L. Andrews, *Structured Light and Its Applications* (Academic, 2008).
14. J. P. Torres and L. Torner, *Twisted Photons* (Wiley-VCH, 2011).
15. D. L. Andrews, *The Angular Momentum of Light* (Cambridge University Press, 2013).
16. E. Komatsu, "Matter Adds Twist to Cosmic Microwave Background," Physics **6**, 107 (2013).
17. D. Hanson et.al., "Detection of B-Mode Polarization in the Cosmic Microwave Background with Data from the South Pole Telescope," Phys. Rev. Lett. **111**, 141301 (2013).
18. J. Lizarraga, J. Urrestilla, D. Daverio, M. Hindmarsh, M. Kunz, and A. R. Liddle, "Can Topological Defects Mimic the BICEP2 B-Mode Signal?," Phys. Rev. Lett. **112**, 171301 (2014).

19. A. Moss and L. Pogosian, "Did BICEP2 See Vector Modes? First B-Mode Constraints on Cosmic Defects," Phys. Rev. Lett. **112**, 171302 (2014).
20. "The power of analogies," Nat. Photonics **8**, 1–1 (2014).
21. D. G. Grier, "A revolution in optical manipulation," Nature **424**, 810–816 (2003).
22. K. Dholakia and T. Čižmár, "Shaping the future of manipulation," Nat. Photonics **5**, 335–342 (2011).
23. K. Lou, S.-X. Qian, Z.-C. Ren, C. Tu, Y. Li, and H.-T. Wang, "Femtosecond Laser Processing by Using Patterned Vector Optical Fields," Sci. Rep. **3**, (2013).
24. K. Toyoda, K. Miyamoto, N. Aoki, R. Morita, and T. Omatsu, "Using Optical Vortex To Control the Chirality of Twisted Metal Nanostructures," Nano Lett. **12**, 3645–3649 (2012).
25. E. M. Kramer and J. V. Groves, "Defect coarsening in a biological system: The vascular cambium of cottonwood trees," Phys. Rev. E **67**, 041914 (2003).
26. V. V. Isaeva, N. V. Kasyanov, and E. V. Presnov, "Topological singularities and symmetry breaking in development," Biosystems **109**, 280–298 (2012).
27. L. S. Hirst, A. Ossowski, M. Fraser, J. Geng, J. V. Selinger, and R. L. B. Selinger, "Morphology transition in lipid vesicles due to in-plane order and topological defects," Proc. Natl. Acad. Sci. **110**, 3242–3247 (2013).
28. P. C. Brady, K. A. Travis, T. Maginnis, and M. E. Cummings, "Polaro–cryptic mirror of the lookdown as a biological model for open ocean camouflage," Proc. Natl. Acad. Sci. **110**, 9764–9769 (2013).
29. A. Y. Bekshaev and M. S. Soskin, "Transverse energy flows in vectorial fields of paraxial beams with singularities," Opt. Commun. **271**, 332–348 (2007).
30. R. Zambrini and S. M. Barnett, "Angular momentum of multimode and polarization patterns," Opt. Express **15**, 15214–15227 (2007).
31. L.-G. Wang, "Optical forces on submicron particles induced by full Poincaré beams," Opt. Express **20**, 20814–20826 (2012).

32. T.-H. Lan and C.-H. Tien, "Manipulation of the Steering and Shaping of SPPs via Spatially Inhomogeneous Polarized Illumination," Opt. Express **18**, 23314–23323 (2010).
33. T.-H. Lan, C.-Y. Ho, and C.-H. Tien, "Direct measurement of versatile surface plasmon polaritons excited by split polarization," Appl. Phys. Lett. **98**, 081107 (2011).
34. S. Pidishety, V. Kumar, and N. K. Viswanathan, "Plasmon-mediated vectorial topological dipole: formation and annihilation," Opt. Lett. **37**, 4233–4235 (2012).
35. J. S. Tyo, D. L. Goldstein, D. B. Chenault, and J. A. Shaw, "Review of passive imaging polarimetry for remote sensing applications," Appl. Opt. **45**, 5453–5469 (2006).
36. G. Milione, T. A. Nguyen, E. Karimi, D. A. Nolan, S. Slussarenko, L. Marrucci, and R. Alfano, "Superdense Coding with Vector Vortex Beams: A Classical Analogy of Entanglement," in *Frontiers in Optics 2013*, OSA Technical Digest (online) (Optical Society of America, 2013), p. FM3F.4.
37. G. Molina-Terriza, J. P. Torres, and L. Torner, "Twisted photons," Nat. Phys. **3**, 305–310 (2007).
38. E. Nagali, L. Sansoni, L. Marrucci, E. Santamato, and F. Sciarrino, "Experimental generation and characterization of single-photon hybrid ququarts based on polarization and orbital angular momentum encoding," Phys. Rev. A **81**, 052317 (2010).
39. N. M. Litchinitser, "Structured Light Meets Structured Matter," Science **337**, 1054–1055 (2012).
40. G. Gbur and T. D. Visser, "The Structure of Partially Coherent Fields," in *Progress in Optics* (Elsevier, 2010), Vol. Volume 55, pp. 285–341.
41. J. Serna and J. M. Movilla, "Orbital angular momentum of partially coherent beams," Opt. Lett. **26**, 405–407 (2001).
42. O. V. Angelsky, M. P. Gorsky, P. P. Maksimyak, A. P. Maksimyak, S. G. Hanson, and C. Y. Zenkova, "Investigation of optical currents in coherent and partially coherent vector fields," Opt. Express **19**, 660–672 (2011).

43. G. Gbur and T. D. Visser, "Coherence vortices in partially coherent beams," Opt. Commun. **222**, 117–125 (2003).
44. W. Wang and M. Takeda, "Coherence Current, Coherence Vortex, and the Conservation Law of Coherence," Phys. Rev. Lett. **96**, 223904 (2006).
45. C. V. Felde, A. A. Chernyshov, G. V. Bogatyryova, P. V. Polyanskii, and M. S. Soskin, "Polarization singularities in partially coherent combined beams," JETP Lett. **88**, 418–422 (2008).
46. A. A. Chernyshov, K. V. Fel'de, G. V. Bogatyreva, P. V. Polyanskii, and M. S. Soskin, "Vector singularities of superposition of mutually incoherent orthogonally polarized beams," Opt. Spectrosc. **107**, 645–650 (2009).
47. I. Georgescu, "Foundations of quantum mechanics," Nat. Phys. **10**, 253–253 (2014).

Appendices

A. Theory of two-mode optical fiber [1]

The vector modes of an optical fiber can be understood by considering the vector wave equation.

$$[\nabla^2 + n^2(x,y)k^2]\vec{E} = -\nabla\left[\vec{E}\cdot\nabla \ln n^2(x,y)\right] \tag{A.1}$$

Here, $k = 2\pi/\lambda$, $n^2(x,y) = n_{co}^2\{1 - 2\Delta f(x,y)\}; n_{cl}^2 = n_{co}^2\{1-2\Delta\}$, where n_{co} and n_{cl} are the refractive index of the core and cladding and $f(x,y)$ determines the distribution of the refractive index profile. For cylindrical symmetric step-index fiber the transverse electric field solutions of the above vector wave equation can be written in the form

$$\vec{E}(x,y,z) = \vec{e}_t(x,y)e^{\{i(\tilde{\beta}+\delta\beta)z\}} \tag{A.2}$$

Where, the propagation constant $\tilde{\beta}$ is a solution of the scalar wave equation $\left[\nabla^2 + n^2k^2 - \tilde{\beta}^2\right]e_t = 0$ and $\delta\beta$ is the correction due to waveguide polarization properties. Therefore, for an ideal two-mode step index optical fiber ($n_{co} = 1.4142, n_{cl} = 1.3999, \rho = 1.911\mu m$) there exists two fundamental Eigen modes which are x and y polarized Gaussian modes and four-first order vector eigen modes as shown in Figure A.1.

$$\begin{aligned}
\vec{E}_{HE_{21}^e} &= F_l(\rho)\left[\{\cos\phi\hat{x} - \sin\phi\,\hat{y}\}e^{\{i(\tilde{\beta}+\delta\beta_1)z\}}\right]\\
\vec{E}_{TM_{01}} &= F_l(\rho)\left[\{\cos\phi\hat{x} + \sin\phi\,\hat{y}\}e^{\{i(\tilde{\beta}+\delta\beta_2)z\}}\right]\\
\vec{E}_{HE_{21}^o} &= F_l(\rho)\left[\{\sin\phi\,\hat{x} + \cos\phi\,\hat{y}\}e^{\{i(\tilde{\beta}+\delta\beta_3)z\}}\right]\\
\vec{E}_{TE_{01}} &= F_l(\rho)\left[\{\sin\phi\,\hat{x} - \cos\phi\,\hat{y}\}e^{\{i(\tilde{\beta}+\delta\beta_4)z\}}\right]
\end{aligned} \tag{A.3}$$

Here $F_l(\rho)$ is the solution of $\left\{\frac{d^2}{d\rho^2} + \frac{1}{\rho}\frac{d}{d\rho}k^2n^2 - \frac{l^2}{\rho^2} - \tilde{\beta}^2\right\}F_l = 0$ for $l = 1$, $\tilde{\beta} = V/\rho(2\Delta)^{1/2}\left\{1 - 2\Delta\frac{\widetilde{U}}{V}\right\}^{1/2}$ is the propagation constant where $V = k\rho\left(n_{co}^2 - n_{cl}^2\right)^{1/2}$, $\widetilde{U} = \rho\left\{k^2n_{co}^2 - \tilde{\beta}^2\right\}^{1/2}$, $V^2 = \widetilde{U}^2 + \widetilde{W}^2$ and corrections to propagation constants are given by $\delta\beta_1 = \delta\beta_3 = -\frac{(2\Delta)^{3/2}}{2\rho}\frac{\widetilde{W}\widetilde{U}^2}{V^3}\frac{K_l(\widetilde{W})}{K_{l-1}(\widetilde{W})}$, $\delta\beta_2 =$

$-\frac{(2\Delta)^{3/2}}{\rho}\frac{\tilde{W}\tilde{U}^2}{V^3}\frac{K_1(\tilde{W})}{K_2(\tilde{W})}$ and $\delta\beta_4 = 0$. There are alternate representations of fiber modes in terms of linearly polarized (LP) or circularly polarized (CP) modes, which can be written as superposition of the vector eigen modes [2,3].

$$\begin{aligned} LP_{11}^{e,x} &= HE_{21}^{e} + TM_{01};\ CP_{11}^{e+} = LP_{11}^{e,x} + iLP_{11}^{e,y} \\ LP_{11}^{o,y} &= HE_{21}^{e} - TM_{01};\ CP_{11}^{o+} = LP_{11}^{o,x} - iLP_{11}^{o,y} \\ LP_{11}^{o,x} &= HE_{21}^{o} + TE_{01};\ CP_{11}^{e-} = LP_{11}^{o,x} - iLP_{11}^{o,y} \\ LP_{11}^{e,y} &= HE_{21}^{o} - TE_{01};\ CP_{11}^{o-} = LP_{11}^{e,x} + iLP_{11}^{e,y} \end{aligned} \tag{A.4}$$

Thus there exists three basis sets for fiber Eigen modes: (1) Vector Eigen modes, (2) linearly polarized Eigen modes and (3) circularly polarized Eigen modes. Therefore any propagating mode inside the fiber can be expressed as a linear superposition of any of the three basis sets.

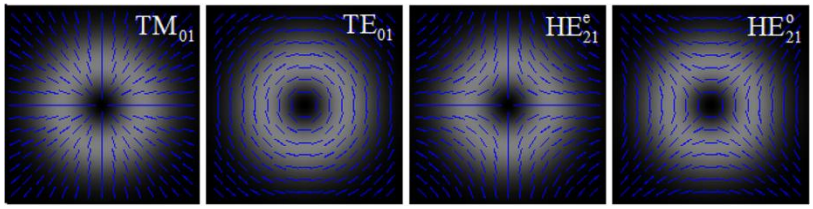

Figure A.1. First higher-order vector modes of the two-mode optical fiber. Linear polarization vibration direction (blue line) is superposed on the gray scale intensity profile of the modes.

B. Stokes polarimetry

B.1. Polarization ellipse parameters and Stokes parameters [4]

A plane wave at the plane $z = 0$ can be represented in real terms and/or in complex term by equations:

$$\begin{aligned} E_x(t) &= E_{0x}(t)\cos[\omega t - \delta_x(t)] = E_x e^{i\omega t} \\ E_y(t) &= E_{0y}(t)\cos[\omega t - \delta_y(t)] = E_y e^{i\omega t} \end{aligned} \tag{B.1}$$

Here $E_{0x}(t)$ and $E_{0y}(t)$ are real amplitudes and $E_x = E_{0x}e^{i\delta_x}$ and $E_y = E_{0y}e^{i\delta_y}$ are complex amplitudes. The explicit removal of the term ωt in real term representation of the Equation (B.1) results in polarization ellipse equation describing all possible states of polarization. Therefore,

$$\frac{E_x^2(t)}{E_{0x}^2(t)} + \frac{E_y^2(t)}{E_{0y}^2(t)} - \frac{2E_x(t)E_y(t)}{E_{0x}(t)E_{0y}(t)}\cos\delta(t) = \sin^2\delta(t) \tag{B.2}$$

where $\delta(t) = \delta_y(t) - \delta_x(t)$ is the phase difference between the orthogonal components in x and y-direction. Multiplying Equation (B.2) by $4E_{0x}^2E_{0y}^2$ and taking the time average $\langle E_i(t)E_j(t)\rangle = \lim_{T\to\infty}\frac{1}{T}\int_0^T E_i(t)E_j(t)dt$. we get,

$$2E_{0x}^2E_{0y}^2 + 2E_{0x}^2E_{0y}^2 - \left(2E_{0x}E_{0y}\cos\delta\right)^2 = \left(2E_{0x}E_{0y}\sin\delta\right)^2 \tag{B.3}$$

Adding and subtracting $E_{0x}^4 + E_{0y}^4$ to the left side of Equation (B.3) will result in perfect square terms and rearranging them gives:

$$\left(E_{0x}^2 + E_{0y}^2\right)^2 = \left(E_{0x}^2 - E_{0y}^2\right)^2 + \left(2E_{0x}E_{0y}\cos\delta\right)^2 + \left(2E_{0x}E_{0y}\sin\delta\right)^2 \tag{B.4}$$

We now introduce the quantities known as *Stokes parameters* defined as:

$$\begin{aligned} S_0 &= E_{0x}^2 + E_{0y}^2 = E_xE_x^* + E_yE_y^* \\ S_1 &= E_{0x}^2 - E_{0y}^2 = E_xE_x^* - E_yE_y^* \\ S_2 &= 2E_{0x}E_{0y}\cos\delta = E_xE_y^* + E_yE_x^* \\ S_3 &= 2E_{0x}E_{0y}\sin\delta = i(E_xE_y^* + E_yE_x^*) \end{aligned} \tag{B.5}$$

Thus the state of polarization can also be represented by Stokes parameters (B.5) in addition to polarization ellipse (B.2). We can write the polarization ellipse parameters: orientation (χ) and ellipticity ($\xi = \pm b/a$) (Figure B.1) using Stokes parameters as,

$$\begin{aligned} \chi &= \frac{1}{2}\tan^{-1}\left(\frac{2E_{0x}E_{0y}\cos\delta}{E_{0x}^2 - E_{0y}^2}\right) = \frac{1}{2}\tan^{-1}\left(\frac{S_2}{S_1}\right) \\ \xi &= \tan\left(\frac{1}{2}\sin^{-1}\left(\frac{2E_{0x}E_{0y}\sin\delta}{E_{0x}^2 + E_{0y}^2}\right)\right) = \tan\left(\frac{1}{2}\sin^{-1}\left(\frac{S_3}{S_0}\right)\right) \end{aligned} \tag{B.6}$$

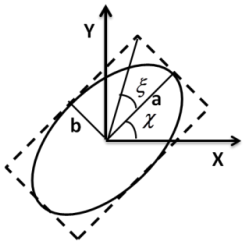

Figure B.1. Polarization ellipse. Semi-minor and semi-major axis represented by "b" and "a" such that ellipticity $\boldsymbol{\xi = b/a}$ and $\boldsymbol{\chi}$ is the ellipse orientation.

B.2. Experimental determination of Stokes parameters [5]

The component of electric field vector making an angle θ with the positive x-direction, after the retardation ε has been introduced, is given by,

$$E = E_x \cos\theta + e^{i\varepsilon} E_y \sin\theta \tag{B.7}$$

and assuming $J_{ji} = J_{ij}^*$ the corresponding intensity $I(\theta, \varepsilon) = \langle EE^* \rangle$ is given by

$$I(\theta, \varepsilon) = J_{xx} \cos^2\theta + J_{yy} \sin^2\theta + 2\sqrt{J_{xx}}\sqrt{J_{yy}} \cos\theta \sin\theta \left| j_{xy} \right| \cos(\beta_{xy} - \varepsilon) \tag{B.8}$$

Here, $J_{xx} = E_x E_x^*$, $J_{xy} = E_x E_y^*$ etc. and $j_{xy} = \left| j_{xy} \right| e^{i\beta_{xy}} = \frac{J_{xy}}{\sqrt{J_{xx}}\sqrt{J_{yy}}}$. Therefore using Equation (B.7) and (B.5), we can get the Stokes parameters in terms of intensities $I(\theta, \varepsilon)$ as,

$$\begin{aligned} S_0 &= I(0°, 0) + I(90°, 0) \\ S_1 &= I(0°, 0) - I(90°, 0) \\ S_2 &= I(45°, 0) - I(135°, 0) \\ S_3 &= I\left(45°, \frac{\pi}{2}\right) - I(135°, \frac{\pi}{2}) \end{aligned} \tag{B.9}$$

Therefore, by using a combination of polarizer and quarter-wave plate we can measure all the six set of intensities $I(\theta, \varepsilon)$ as required to construct the Stokes parameters using (B.9) thereby we can draw the polarization ellipse to completely characterize the state of polarization.

B.3. Stokes parameters and topological optics

Once the Stokes parameters are known the topological optics is simply the algebra of Stokes parameters. Thus, first we define the Stokes field (S_{ij}) and the corresponding Stokes (Poincaré) vortices (Φ_{ij}) [6,7] as,

$$\begin{aligned} S_{12} &= S_1 + iS_2 \Rightarrow \Phi_{12} = \arg(S_1 + iS_2) \\ S_{23} &= S_2 + iS_3 \Rightarrow \Phi_{23} = \arg(S_2 + iS_3) \\ S_{31} &= S_3 + iS_1 \Rightarrow \Phi_{31} = \arg(S_3 + iS_1) \end{aligned} \tag{B.10}$$

Actually the C-point singularity is the Stokes vortex Φ_{12} and can be found as $S_1 + iS_2 = 0$. The L-line singularity is determined by setting $S_3 = 0$. The streamlines in the ellipse orientation field (or any other parameter field) are

the family of solutions of the differential equation $dy/dx = \sin\chi / \cos\chi$, which forms the topological structure around the singular point.

As we can see from the Equation (B.9) and (B.5), Φ_{23} represents the phase difference between the orthogonal components represented by S_1, and therefore Φ_{23} can be used to extract the non-plane phase of the scalar beams [8,9]. But in general Φ_{ij} is the phase-difference between the components of S_k where $i, j, k = 1,2,3$ goes in cyclic combination [9].

References

1. A. W. Snyder and J. D. Love, *Optical Waveguide Theory* (Chapman & Hall, 1991).
2. A. V. Volyar and T. A. Fadeeva, "Optics of Singularities of the Field of a Low-Mode Fiber:I. Circular Disclinations," Opt. Spectrosc. **85**, 264–271 (1998).
3. A. V. Volyar and T. A. Fadeeva, "Optics of Singularities of a Low-Mode Fiber: II. Optical Vortices," Opt. Spectrosc. **85**, 272–280 (1998).
4. D. H. Goldstein, *Polarized Light*, 2nd ed. (CRC Press, 2003).
5. M. Born and E. Wolf, *Principles of Optics*, 7th ed. (Cambridge University Press, 1999).
6. I. Freund, "Poincaré vortices," Opt. Lett. **26**, 1996–1998 (2001).
7. I. Freund, A. I. Mokhun, M. S. Soskin, O. V. Angelsky, and I. I. Mokhun, "Stokes singularity relations," Opt. Lett. **27**, 545–547 (2002).
8. V. Kumar and N. K. Viswanathan, "Topological structures in the Poynting vector field: an experimental realization," Opt. Lett. **38**, 3886–3889 (2013).
9. V. Kumar and N. K. Viswanathan, "Topological structures in vector-vortex beam fields," J. Opt. Soc. Am. B **31**, A40 (2014).

List of Publications

Journal Papers

1) **Vijay Kumar** and Nirmal K. Viswanathan, "Topological structures in vector-vortex beam fields" J. Opt. Soc. Am. B 31, A40-A45 (2014).
2) Enrique J. Galvez , Brett L. Rojec, **Vijay Kumar** and Nirmal K. Viswanathan, "Generation of asymmetric umbilics in light's polarization" Phys. Rev. A, 89, 031801(R) (2014).
3) **Vijay Kumar** and Nirmal K. Viswanathan, "Topological structures in Poynting vector field: An Experimental realization" Opt. Lett. 38, 3886-3889, 2013.
4) **Vijay Kumar**, Geo M. Philip and Nirmal K. Viswanathan, "Formation and Morphological Transformation of Polarization Singularities: Hunting the Monstar" *J. Opt.* 15, 044027, 2013.
5) **Vijay Kumar** and Nirmal K. Viswanathan, "Pancharatnam-Berry phase in polarization singular beams" *J. Opt.* 15, 044026, 2013.
6) Shankar Pidishety, **Vijay Kumar** and Nirmal K. Viswanathan, "Plasmon-mediated Vectorial Topological Dipole: Formation and Annihilation" Opt. Lett. 37, 4233-4235 (2012).
7) **Vijay Kumar**, V.V.G. Krishna Inavalli and Nirmal K. Viswanathan, "Dynamic Evolution of Transverse Energy Flow in Focused Asymmetric Optical Vector-Vortex Beams" Opt. Comm. 285, 4866-4873 (2012).
8) Geo M. Philip, **Vijay Kumar**, Giovanni Milione, and Nirmal K. Viswanathan, "Manifestation of the Gouy phase in vector-vortex beams" Opt. Lett. 37, 2667-2669 (2012).

Magazine article

1) Nirmal K. Viswanathan and **Vijay Kumar,** "Angular momentum of light" Kiran: A Bulletin of Indian laser association, Vol.24, Iss.03, 20-25(2013).

TOPOLOGICAL OPTICS: STRUCTURED BEAM-FIELDS

Conference and Workshop Papers

Oral Presentation

1) **Vijay Kumar** and Nirmal K. Viswanathan, "Topological aspects of polarization structured beams" Proc. of SPIE Vol. 8999, 89990M, 2014.
2) **Vijay Kumar** and Nirmal K. Viswanathan, "Poynting vector of complex optical field" FW4F.5, Frontiers in optics, Orlando, Florida, USA 2013.
3) **Vijay Kumar** and Nirmal K. Viswanathan, "Polarization singularities and fiber modal decomposition" Proc. of SPIE Vol. 8637, 86371A, 2013.
4) **Vijay Kumar**, Giovanni Milione and Nirmal K. Viswanathan, "Geometric phase in anisotropic polarization singular fields" 5th International Conference on Singular Optics, Sevastopol, Ukraine 2012
5) **Vijay Kumar** and Nirmal K. Viswanathan, "Dynamical properties optical vortex beam with tunable anisotropy" International Conference on Contemporary Trends in Optics and Opto Electronics, Thiruvananthapuram, India, 2011.

Poster Presentations

6) **Vijay Kumar** and Nirmal K. Viswanathan, "Topological optics" Workshop on recent advances in photonics (WRAP), IIT Delhi, India 2013.
7) **Vijay Kumar**, Giovanni Milione and Nirmal K. Viswanathan, "Monstardom Sphere" International workshop on Singularities and topological structures of light. ICTP Trieste, Italy, 2013.
8) **Vijay Kumar** and Nirmal K. Viswanathan, "Measuring Poynting vector of optical vortices using polarization interference " Second International Conference on Optical Angular Momentum , The Burrell collection, Glasgow, UK 2013.
9) **Vijay Kumar**, V.V.G. Krishna Inavalli and Nirmal K. Viswanathan, "Wavelength-dependent spin-orbit interaction in optical fiber" International workshop on spin-orbit interaction for light and matter waves, MPIPKS Dresden, Germany 2013.

TOPOLOGICAL OPTICS: STRUCTURED BEAM-FIELDS

10) **Vijay Kumar** and Nirmal K. Viswanathan, "Evolution of polarization singularities in few-mode fiber" WPo.22, International Conference on Fiber Optics and Photonics, Chennai, India 2012
11) Shankar Pidishety, **Vijay Kumar** and Nirmal K. Viswanathan, "Plasmon-mediated Vectorial Topological Dipole" FTu3A.31, Frontiers in optics, Rochester, USA 2012.

This thesis is devoted to singularities in π-symmetric (line) and 2π-symmetric (vector) fields. Singularities in line fields are associated with fundamental ½-index topological structures: lemon, monstar and star. Whereas, radial, node, spiral, circulation and saddle are index-one fundamental topological structures associated with singularities in vector field. Analogous to the Poincaré sphere, topological sphere of ½-index and index-one are theoretically constructed and experimentally realized. These spheres represent all possible symmetric and asymmetric structures achievable in the respective fields, on the surface of the sphere. The ½-index fundamental structures are experimentally realized in the polarization ellipse orientation field using optical fiber and free-space interferometers. Whereas, index-one fundamental structures are experimentally realized in the Poynting vector field, linearly polarized field as well as in the polarization ellipse orientation field. Manifestation of the Pancharatnam-Berry phase and the Gouy phase in polarization topological structured beam-fields are also studied. In addition, the direct and indirect measurements of the Poynting vector in structured beam-fields containing various polarization singularities such as C-point, dipole, C-line are also explored.